Article

Molecular Cell

Multidomain Convergence of Argonaute during RISC Assembly Correlates with the Formation of Internal Water Clusters

Graphical Abstract

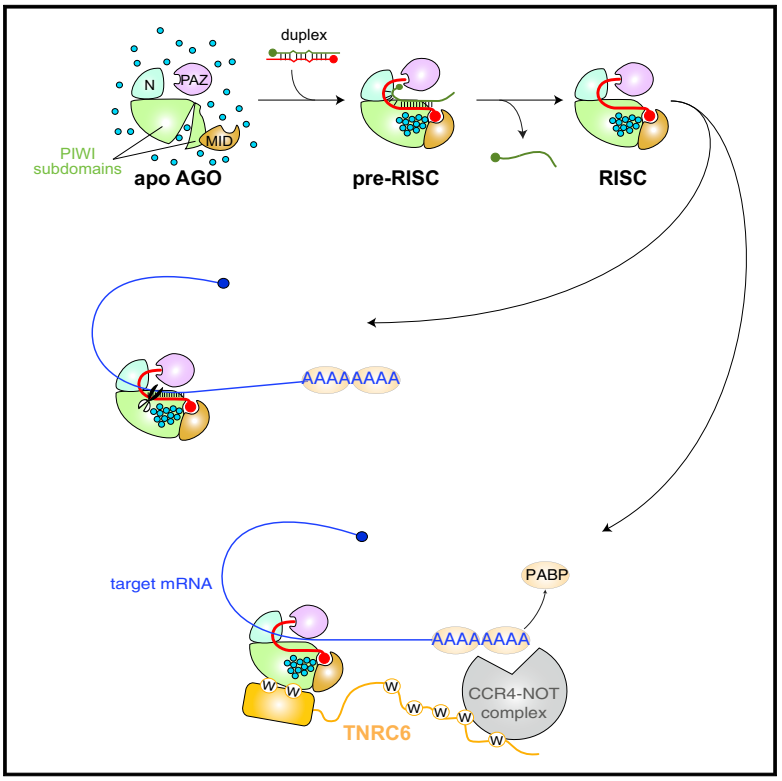

Highlights

- Crystal structure of AGO4-RISC completes the structural catalogs of four human AGOs
- Guide RNA binding ties together two PIWI subdomains and allows the RISC to bind TNRC6
- Confining water molecules inside AGO is essential to form functional RISC
- Interior water clusters named LAKEs are conserved in AGOs but not in PIWIs

Authors

Mi Seul Park, Raul Araya-Secchi, James A. Brackbill, ..., Daniel M. Dayeh, Marcos Sotomayor, Kotaro Nakanishi

Correspondence

nakanishi.9@osu.edu

In Brief

Park et al. present the crystal structure of human Argonaute4 bound to guide RNA, revealing water molecules that form two clusters and that tie together its converged domains to stabilize the bilobal RISC scaffold. This water reservoir formation essential for duplex loading is common among Argonaute proteins but not PIWIs.

Park et al., 2019, Molecular Cell *75*, 725–740
August 22, 2019
https://doi.org/10.1016/j.molcel.2019.06.011

CellPress

Molecular Cell
Article

Multidomain Convergence of Argonaute during RISC Assembly Correlates with the Formation of Internal Water Clusters

Mi Seul Park,[1,2,7] Raul Araya-Secchi,[1,5,7] James A. Brackbill,[1,2,7] Hong-Duc Phan,[2,3,7] Audrey C. Kehling,[1,2] Ekram W. Abd El-Wahab,[1,2,6] Daniel M. Dayeh,[1,2,3] Marcos Sotomayor,[1,3,4] and Kotaro Nakanishi[1,2,3,8,*]
[1]Department of Chemistry and Biochemistry, The Ohio State University, Columbus, OH 43210, USA
[2]Center for RNA Biology, The Ohio State University, Columbus, OH 43210, USA
[3]Ohio State Biochemistry Program, The Ohio State University, Columbus, OH 43210, USA
[4]Biophysics Graduate Program, The Ohio State University, Columbus, OH 43210, USA
[5]Present address: Structural Biophysics, X-Ray and Neutron Science, Niels Bohr Institute, University of Copenhagen, 2100 Copenhagen, Denmark
[6]Present address: Tropical Health Department, High Institute of Public Health, Alexandria University, Alexandria 21561, Egypt
[7]These authors contributed equally
[8]Lead Contact
*Correspondence: nakanishi.9@osu.edu
https://doi.org/10.1016/j.molcel.2019.06.011

SUMMARY

Despite the relevance of Argonaute proteins in RNA silencing, little is known about the structural steps of small RNA loading to form RNA-induced silencing complexes (RISCs). We report the 1.9 Å crystal structure of human Argonaute4 with guide RNA. Comparison with the previously determined apo structure of *Neurospora crassa* QDE2 revealed that the PIWI domain has two subdomains. Binding of guide RNA fastens the subdomains, thereby rearranging the active-site residues and increasing the affinity for TNRC6 proteins. We also identified two water pockets beneath the nucleic acid-binding channel that appeared to stabilize the mature RISC. Indeed, mutating the water-pocket residues of Argonaute2 and Argonaute4 compromised RISC assembly. Simulations predict that internal water molecules are exchangeable with the bulk solvent but always occupy specific positions at the domain interfaces. These results suggest that after guide RNA-driven conformational changes, water-mediated hydrogen-bonding networks tie together the converged domains to complete the functional RISC structure.

INTRODUCTION

Humans have four Argonaute paralogs (AGO1–AGO4). They load microRNAs (miRNAs) to form RNA-induced silencing complexes (RISCs) that target complementary mRNAs for gene silencing (Bartel, 2018; Kobayashi and Tomari, 2016). RNA sequencing analyses revealed a large overlap of small RNAs between different AGOs, with a limited population of small RNAs unique to each AGO (Azuma-Mukai et al., 2008; Beitzinger et al., 2007; Dueck et al., 2012; Hafner et al., 2010), suggesting the redundancy and specificity of their target mRNAs. To date, characteristic features of each AGO have been reported. For example, AGO1 interacts with RNA polymerase II bound to the active promoters (Huang et al., 2013) and controls alternative splicing through transcriptional enhancers (Alló et al., 2014). Only AGO2 cleaves precursor miR-451 and generates the mature miRNA important for erythropoiesis (Cheloufi et al., 2010). AGO3 shares the same catalytic tetrad with AGO2, but activation for RNA cleavage requires specific guides (Park et al., 2017b). AGO4 regulates entry into meiosis and influences silencing of sex chromosomes in male mouse germlines (Modzelewski et al., 2012) and is exploited for the replication of hepatitis delta virus (Haussecker et al., 2008). To elucidate the molecular bases for the common and unique roles of each AGO, a comprehensive structural comparison is indispensable. The previously determined RISC structures of AGO1, AGO2, and AGO3 showed their unique local structures (Elkayam et al., 2012; Faehnle et al., 2013; Nakanishi et al., 2013; Park et al., 2017b; Schirle and MacRae, 2012). In contrast, no structural information is currently available for AGO4, although a model structure was proposed (Hauptmann et al., 2014).

Since the discovery of RNAi (Fire et al., 1998), tremendous advancements have identified the miRNA biogenesis pathways, along with its key players. The genes of miRNAs are transcribed and processed by a complex of RNase III enzyme Drosha and DGCR8 in the nucleus (Lee et al., 2003) and by Dicer in the cytoplasm (Bernstein et al., 2001; Zhang et al., 2002). Last, miRNA duplexes are loaded into AGOs (Gregory et al., 2005; MacRae et al., 2008). This loading step requires chaperone machinery, showing drastic conformational changes of AGOs coupled with ATP hydrolysis (Iwasaki et al., 2010, 2015a). In contrast, the subsequent passenger-strand ejection is thermodynamically favored and managed by AGO alone (Kawamata et al., 2009). Thus, the loading step is known to involve drastic AGO conformational changes, but details of AGO's structural transitions during RISC assembly are still poorly understood.

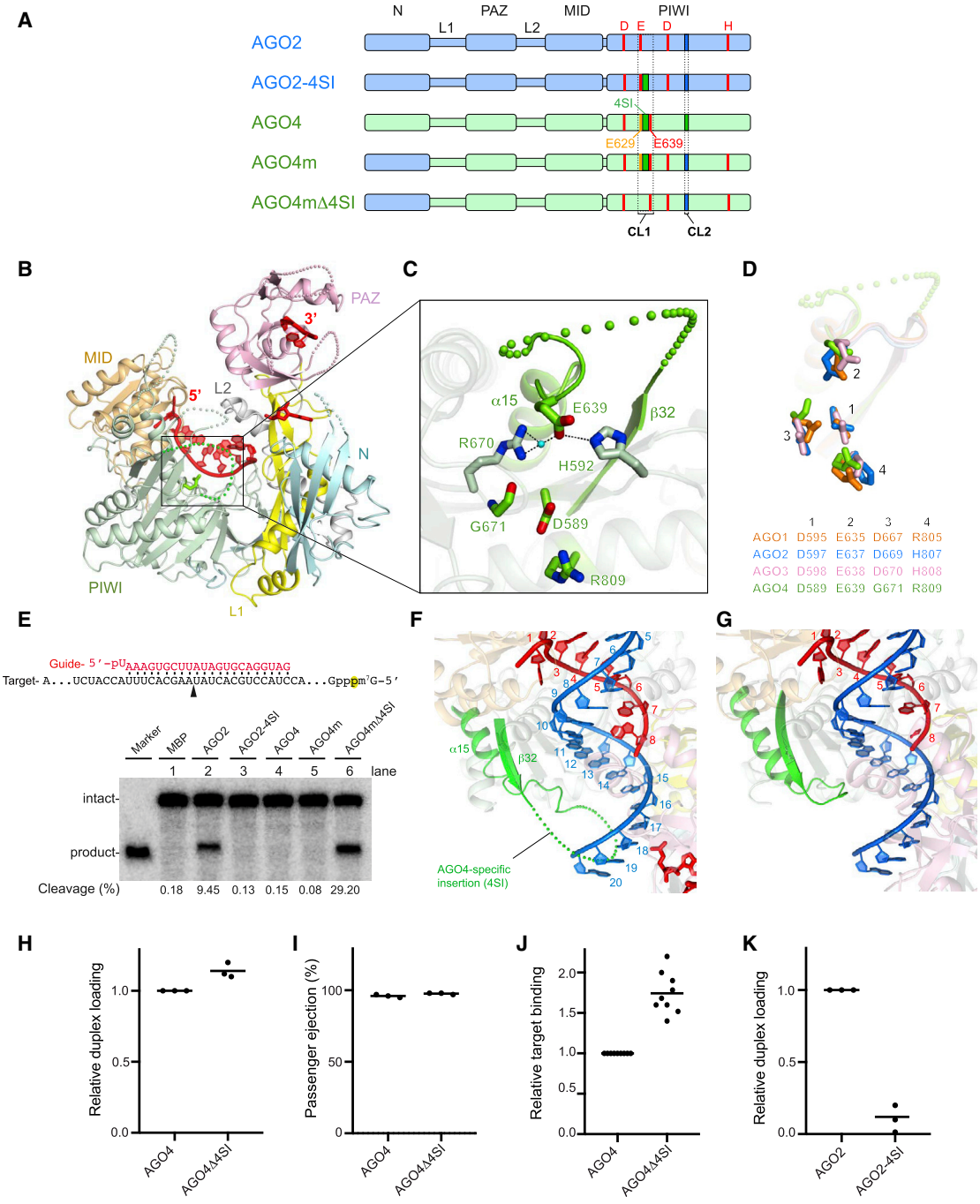

Figure 1. Structure of Human AGO4-RISC

(A) Domain architectures of AGO2 (light blue), AGO4 (light green), and their chimeras. The catalytic residues are shown in red. 4SI within CL1 is colored green. AGO2- and AGO4-specific CL2s are highlighted in blue and green, respectively. The previously proposed glutamate finger of AGO4, E629, is colored yellow.

(B) Overall structure of guide-bound AGO4 with the N (cyan), L1 (yellow), PAZ (pink), L2 (gray), MID (wheat), and PIWI (green) domains. The bound guide RNA is colored red.

(C) A blow-up of the pseudo-catalytic tetrad of AGO4.

(D) Catalytic and pseudo-catalytic tetrads of four human AGOs.

(E) Target cleavage assay with AGO2, AGO4, and their chimeras shown in (A). See also Figure S1C.

(F and G) A docked target or passenger strand (blue) on the current AGO4-RISC (F) and the previously determined AGO2-RISC (PDB ID: 4OLA) (G). See also Figure S1D.

(legend continued on next page)

Previous structural studies have dissected the bilobal RISC scaffold (Nakanishi, 2016). The C-terminal lobe consists of MID and PIWI domains, while the N-terminal lobe is composed of N, L1, PAZ, and L2 domains (conventionally L1 and L2 have been named "linkers," but we label them "domains" here) (Figure 1A). The N-terminal lobe is essential for the catalytic C-terminal lobe to modulate the slicing activity when there is a mismatch between the guide and target strands (Dayeh et al., 2018). There are two regions within the PIWI domain, labeled cluster 1 (CL1) and cluster 2 (CL2), which are known to affect the catalytic activity of AGOs (Hauptmann et al., 2013). Both lobes, which form globular structures with mainly α helices and β strands, are connected by a hinge portion in which loops and domain linkers shape the intervening nucleic acid-binding channel. Although one of these loops can be phosphorylated at Ser798 (Rüdel et al., 2011), this residue is not accessible in the bilobal RISC structure (Nakanishi, 2016), suggesting that the loop must be solvent accessible before AGO incorporates a guide RNA.

Apo human AGO2 is known to be proteolyzed into several fragments but resistant after loading a guide RNA (Elkayam et al., 2012). A recent single-molecule Förster resonance energy transfer (FRET) study revealed that apo fly Ago2 takes many different conformations, but after loading guide RNA, the structure is restricted to a unique conformation (Tsuboyama et al., 2018). These results suggest that a bound guide RNA stitches all of the AGO domains together, likely stabilizing the bilobal structure. Meanwhile, recent studies revealed that extensive pairing between guide RNA and non-canonical target RNAs strips the guide from AGO (De et al., 2013; Park et al., 2017a). Thus, RISCs work as stable effector complexes and retain control of guide RNA release. The molecular mechanism behind RISC disassembly remains elusive.

Here, we report the 1.9 Å crystal structure of human AGO4 in complex with guide RNA. The high-resolution structure enabled us to locate pockets with many water molecules trapped in the protein interior. These water pockets are also found in high-resolution structures of other AGOs. Our combined approach of molecular dynamics (MD) simulation and functional analyses suggests that internal water molecules in these pockets confer structural integrity to all AGOs and presumably facilitate reversible conformational changes, which are essential for RISC function.

RESULTS

Structure of AGO4 Reveals Its True Glutamate Finger

Among the four human AGO paralogs, AGO2 and AGO3 are the only catalytically active enzymes (Liu et al., 2004; Meister et al., 2004; Park et al., 2017b). Both RISC structures share the same conformation in which their second catalytic residue, known as a "glutamate finger," is arranged to complete the catalytic DEDH tetrad (Elkayam et al., 2012; Park et al., 2017b; Schirle and MacRae, 2012). Despite its slicing deficiency, the RISC structure of AGO1 shows the same conformation with its pseudo-catalytic DEDR tetrad (Faehnle et al., 2013; Nakanishi et al., 2013). Because of a lack of structural information, it remains unclear whether the same is true for AGO4, another slicing-deficient paralog. A model structure of AGO4, based on the crystal structure of AGO2, suggested that E629 of AGO4 served as the glutamate finger (Hauptmann et al., 2014). Indeed, AGO4 was successfully converted into a catalytic enzyme (AGO4mΔ4SI′) when part of CL1 within the PIWI domain, S631-V640, was deleted while the N domain, the third and fourth catalytic residues, and CL2 were swapped with their counterparts in AGO2 (Figure S1A, bottom left). Accordingly, E629 and the adjacent S631-V640 region were proposed to be the glutamate finger and the AGO4-specific insertion (4SI′), respectively (Hauptmann et al., 2014).

In this context, we determined the 1.9 Å crystal structure of human AGO4 in complex with guide RNA that was co-purified from insect cells (Figures 1B and S1B; Table 1). This RISC structure shows that AGO4 forms a pseudo-catalytic DEGR tetrad with D589, E639, G671, and R809 (Figure 1C). Structural alignment revealed that E639 occupied the position of the corresponding glutamate finger in other human AGOs (Figure 1D) (Elkayam et al., 2012; Faehnle et al., 2013; Nakanishi et al., 2013; Park et al., 2017b; Schirle and MacRae, 2012). This observation was not consistent with the model structure, in which E629 was assigned as the glutamate finger (Hauptmann et al., 2014). To investigate the role of E639, we converted AGO4 into an active slicer. First, we swapped the N domain, the third and fourth catalytic residues, and the CL2 of AGO4 with the counterparts of AGO2, as previously reported (Figures 1A and S1A) (Hauptmann et al., 2014). The resultant chimera (FLAG-AGO4m) purified from HEK293T cells did not show slicing activity (Figure 1E, lane 5). However, further removal of E629-Q638 (AGO4-specific insertion [4SI]) conferred significant slicing activity (AGO4mΔ4SI) (Figures 1A, 1E [lane 6], and S1A [bottom right]). Thus, our structural and functional studies demonstrate that E639 serves as the glutamate finger of AGO4, while the region E629-Q638 is the actual 4SI.

The AGO4-Specific Insertion May Modulate Target RNA Recognition

The current structure showed clear, continuous electron density maps of the bound guide RNA at nucleotide positions 1–8 (g1–g8) and the 3′ end 1–2 nt, whereas the middle portion was disordered except for a single nucleotide (Figure S1B). This observation indicates that AGO4 recognizes guide RNA similarly to other human AGOs (Elkayam et al., 2012; Faehnle et al., 2013; Nakanishi et al., 2013; Park et al., 2017b; Schirle and MacRae, 2012), except that a 19 residue loop between β32 and α15, including 4SI, protruded toward the nucleic acid-binding channel (Figures 1B and 1C). When an ideal A-form RNA, mimicking a guide-passenger or guide-target duplex, was manually docked on the g2–g7 of AGO4-bound guide RNA, 4SI seemed to

(H and I) Duplex loading (H) and passenger ejection (I) of AGO4 and AGO4Δ4SI. See also Figure S1E.
(J) Target binding to AGO4 and AGO4Δ4SI. See also Figure S1F.
(K) Duplex loading of AGO2 and AGO2-4SI. See also Figure S1G.
Black bars in (H)–(K) represent averages with independent replicates shown as dots.

Table 1. Data Collection and Refinement Statistics

	AGO4-RISC (PDB: 6OON)
Data collection	
Space group	*C*2
Cell dimensions	
a, *b*, *c* (Å)	213.98, 68.01, 83.27
α, β, γ (°)	90.0, 102.7, 90.0
Resolution (Å)	72.26–1.90
R_{pim}	0.047 (0.394)
$I/\sigma I$	10.3 (2.1)
Completeness (%)	99.1 (98.4)
Redundancy	4.1 (4.2)
Refinement	
Resolution (Å)	49.08–1.90
No. reflections	91128
R_{work}/R_{free}	0.171/0.202
No. atoms	
Protein	6314
RNA	243
Water	464
B-factors	
Protein	47.05
RNA	69.30
Water	44.23
RMSDs	
Bond lengths (Å)	0.008
Bond angles (°)	1.117
Ramachandran plot	
Favored (%)	96.88
Allowed (%)	2.73
Disallowed (%)	0.39

RMSD, root-mean-square deviation.

interfere with the interaction between the two strands (Figure 1F). In contrast, the counterpart in AGO2 has a kink-turn (~9 residues) that is too short to contact the docked strand (Figure 1G). These observations prompted us to hypothesize that 4SI affects RISC assembly, guide-dependent target recognition, or both.

To test this idea, we removed 4SI from AGO4 (AGO4Δ4SI) and used this mutant in a RISC maturation assay (see STAR Methods) (Iwasaki and Tomari, 2018). AGO4Δ4SI showed comparable abilities of duplex loading and passenger ejection (Figures 1H and 1I). On the other hand, our filter binding assay indicated that AGO4Δ4SI bound to target RNA more efficiently than the wild-type (WT; Figure 1J). Therefore, the 4SI within AGO4 is not necessary for RISC assembly, but it modulates the guide-dependent target recognition. Reciprocally, when 4SI was implanted at the corresponding position of FLAG-AGO2 (AGO2-4SI) (Figure 1A), the mutant completely lost slicing activity (Figure 1E, lane 3). To examine whether the cleavage deficiency was due to the impact of 4SI on duplex loading or passenger ejection, we performed the RISC maturation assay. AGO2-4SI showed very low duplex loading (Figure 1K), indicating that the implantation of 4SI alone is devastating to RISC maturation of AGO2. This could explain why the mutant showed no RNA cleavage (Figure 1E, lane 3). Altogether, these results suggest that 4SI modulates target RNA recognition by AGO4.

Previous structural studies revealed that AGO1 and AGO3 possess unique local structures, CL2 (also known as cS7) and AGO3-specific insertion (3SI), respectively (Faehnle et al., 2013; Nakanishi et al., 2013; Park et al., 2017b). Like 4SI, CL2 and 3SI protrude toward the nucleic acid-binding channel, which affects the interaction between the middle portions of a guide RNA and its target RNAs. The differences in those AGO-specific motifs suggest that the four human AGOs recognize the middle part of a guide RNA in different manners. Therefore, all four paralogs loaded with the same guide RNA may have different specificities and affinities for target RNAs, which could explain the previously reported specialized roles of each AGO (Haussecker et al., 2008; Hu et al., 2012; Modzelewski et al., 2012; Winter and Diederichs, 2013). Intriguingly, the N domain that does not contain any of the catalytic residues needed to be swapped to generate a catalytic AGO4mΔ4SI (Figure 1E). Because the N domain and the abovementioned AGO-specific motifs on the C-terminal lobe sandwich the middle part of the guide, their specific combinations may be necessary to confer catalytic activity.

Requirements of TNRC6 Proteins for Binding to AGOs

Human AGOs bind to trinucleotide repeat containing six proteins, TNRC6A, TNRC6B, and TNRC6C, to form miRNA-mediated RISCs that degrade target mRNAs by recruiting a CCR4-NOT complex (Baillat and Shiekhattar, 2009; Huntzinger and Izaurralde, 2011; Jakymiw et al., 2005; Jonas and Izaurralde, 2015; Liu et al., 2005a, 2005b). TNRC6 proteins interact with AGOs using their N-terminal region, which includes more than 30 tryptophan residues. The regions called motif I, motif II, and AGO hook are especially known as strong AGO-binding sites (Hauptmann et al., 2015; Lazzaretti et al., 2009; Pfaff et al., 2013). A recent structural study identified three tryptophan-binding pockets on the surface of the AGO2 PIWI domain (Figure 2A) (Sheu-Gruttadauria and MacRae, 2018). Pockets 1 and 2 are used to interact with TNRC6B motif II, while pockets 1 and 3 are required for binding to TNRC6B motif I (Figure S2A) (Sheu-Gruttadauria and MacRae, 2018). Another structural study showed that through its pockets 1 and 2, AGO1 binds to the AGO hook of TNRC6A (Elkayam et al., 2017). Our current structure showed that AGO4 forms the corresponding pockets composed of the same set of residues, except for G612 in pocket 2 and R701 in pocket 3, which are substituted for alanine and glutamine, respectively, in the other paralogs (Figures 2B and S3).

To test if AGO4 binds to specific regions within TNRC6 proteins in a similar manner as does AGO2, we made two TNRC6B fragments, 599–683 and 869–916, including motifs I and II, respectively (Figure S2A) (Pfaff et al., 2013; Sheu-Gruttadauria and MacRae, 2018). We also designed three other fragments, 507–598, 684–770, and 771–860, none of which includes the known strong AGO-binding sites. Because of low solubility, these fragments were expressed as SUMO-tag fused proteins and purified from *E. coli* cells. After preincubation with either of the TNRC6B fragments, AGO2 or AGO4 was analyzed for

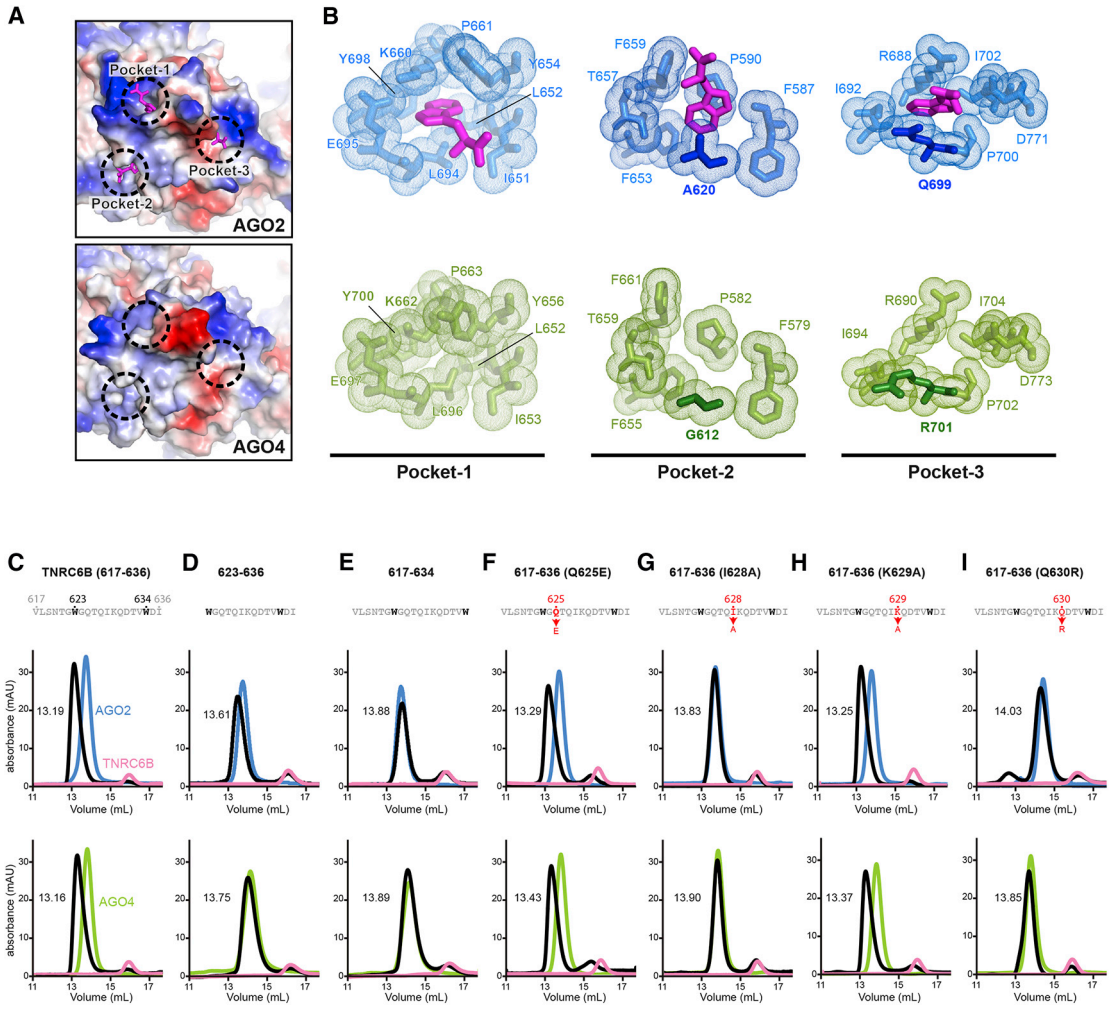

Figure 2. Requirements of TNRC6 for AGO Binding

(A) Electrostatic surfaces of three Trp-binding pockets on the PIWI domain of AGO2 (top; PDB ID: 6CBD) and AGO4 (bottom).

(B) Residues forming the Trp-binding pockets of AGO2 in complex with tryptophans (pink) (top) and apo-AGO4 (bottom).

(C–I) Gel filtration chromatography elution profiles are shown for individual samples of AGO2 (blue), AGO4 (green), and TNRC6B fragment (pink) of 617-636 (C), 623-636 (D), 617-634 (E), 617-636 (Q625E) (F), 617-636 (I628A) (G), 617-636 (K629A) (H), and 617-636 (Q630R) (I), or a preincubated mixture (black) of the TNRC6B fragment and either AGO2 or AGO4.

binding by size exclusion chromatography. Both AGOs interacted only with the two motif-containing TNRC6B fragments, 599–683 and 869–916 (Figure S2B). These results indicated that, despite the differences in pockets 2 and 3, AGO4 distinguishes motifs I and II from other tryptophan repeat regions.

Previous studies reported that AGO1 and AGO2 recognize TNRC6 proteins by binding to two tryptophan residues within AGO-binding sites (Elkayam et al., 2017; Pfaff et al., 2013). The two tryptophans need to be separated by ten amino acids or longer so that they occupy their binding pockets at the same time (Pfaff et al., 2013). However, in the N-terminal domain of TNRC6 proteins, many segments meet the requirements for a strong AGO-binding site. Nevertheless, our present study, as well as others, revealed that human AGOs recognize only specific tryptophan repeat motifs (Figure S2B) (Elkayam et al., 2017; Pfaff et al., 2013; Sheu-Gruttadauria and MacRae, 2018). These results indicate a possibility that motif I, motif II, and AGO hook must possess as yet unidentified determinants that make them different from other tryptophan repeat motifs. To validate this idea, we tested the influence of residues in the vicinity of two tryptophans, W623 and W634, on the AGO binding of the TNRC6B V617-I636 fragment, including its well-studied motif (Hauptmann et al., 2015; Pfaff et al., 2013). The V617-I636 fragment bound to AGO4 as well as AGO2 did (Figure 2C). Deletion of either region outside the two tryptophans, V617-G622 or D635-I636, dramatically affected the binding to AGO2 or AGO4 (Figures 2D and 2E). These results demonstrate the significance of the flanking regions outside a two tryptophan-including segment for binding to AGO. We also made single mutations to residues located between the two tryptophans. Although both Q625E and K629A mutants bound to AGO2 and AGO4 comparably to the WT, the I628A mutant interacted with neither

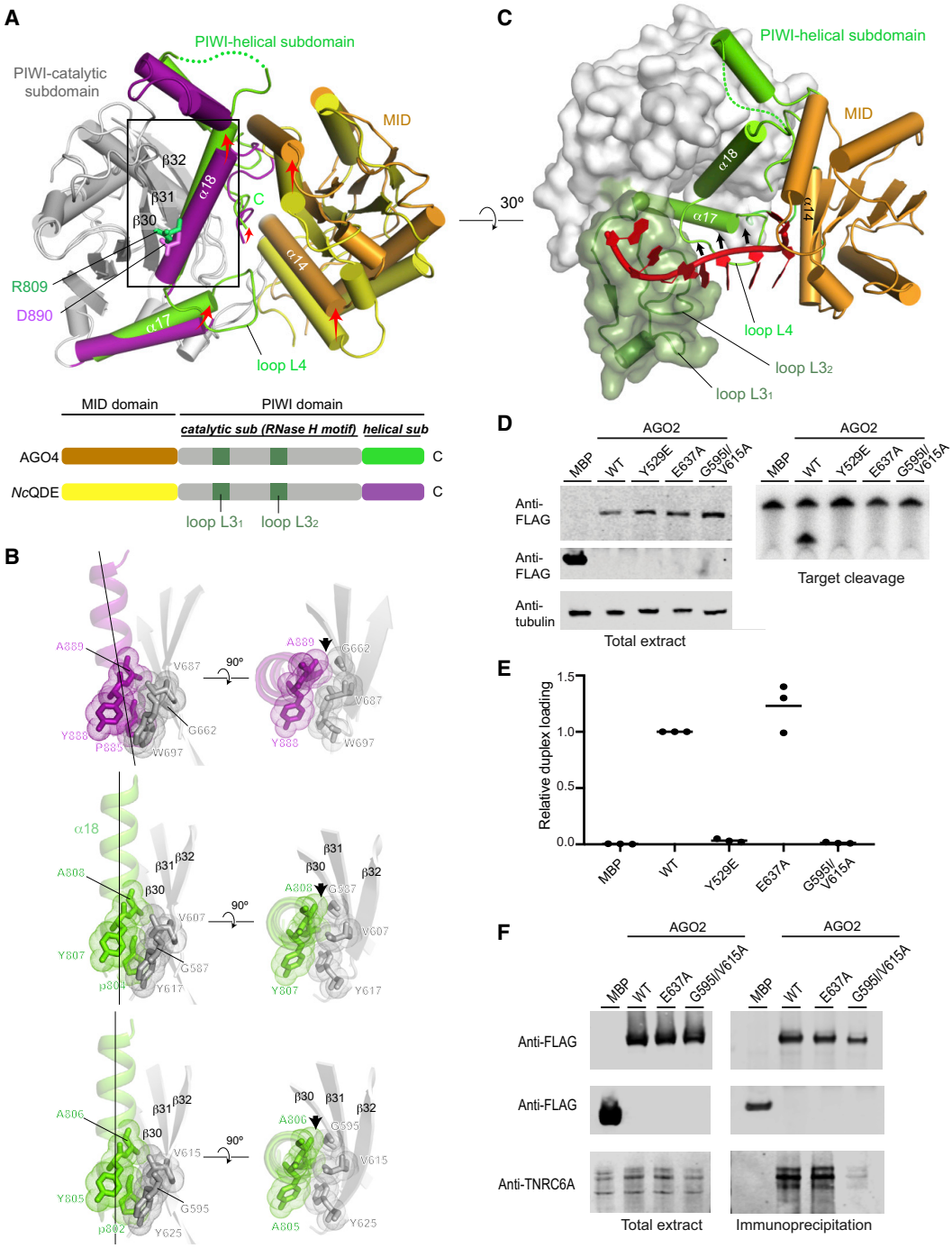

Figure 3. Rearrangement of PIWI Subdomains during RISC Assembly

(A) Different arrangements of PIWI-helical subdomain and MID domain. (Top) The crystal structures of the guide-bound AGO4 and the apo-form *Nc*QDE2 (PDB ID: 2YHA) are superimposed on their PIWI-catalytic subdomains (gray). The pseudo-catalytic residue of AGO4, R809 (green), and the catalytic residue of *Nc*QDE2, D890 (pink), are depicted as a stick model on α18 (see also Figure 1D). The transition from the apo-*Nc*QDE2 to that of the guide-bound AGO4 is shown by red arrows. For clarity, loops $L3_1$ and $L3_2$ and the N-PAZ lobe of AGO4 are not shown. (Bottom) Schematic of the MID and PIWI domains.

(B) Interactions between the two PIWI subdomains of *Nc*QDE2 (top), AGO4 (middle), and AGO2 (bottom). Residues involved in the hydrophobic interaction are shown as stick models with their van der Waals radii (dots). Colors as in (A).

(C) Seed region of guide RNA tying together two PIWI subdomains of AGO4. For clarity, the N-PAZ lobe is not shown. The PIWI-catalytic subdomain is shown as a surface model. The MID domain and the PIWI-helical subdomain are depicted as ribbon models. The guide RNA is colored in red. Colors as in (A).

(legend continued on next page)

(Figures 2F–2H). Given that the corresponding residue in TNRC6 protein homologs and paralogs (i.e., GW182 proteins) is isoleucine or valine, a β-branched, non-polar residue at position 628 seems to be essential for the motif I to interact with AGOs. When a strictly conserved Q630 was replaced with arginine, the mutant completely lost the ability to bind to AGO2 or AGO4 (Figure 2I). These results indicate that the flanking regions outside of and the specific residues between two tryptophan residues are also determinants of AGO-binding sites.

Two PIWI Subdomains Fasten Together upon RNA Binding

A previous study determined the RNA-free structure of the C-terminal lobe of the *Neurospora crassa* Argonaute homolog QDE2 (*Nc*QDE2 C-lobe), which is the only structure reflecting the apo form of a eukaryotic Argonaute protein thus far (Boland et al., 2011). To investigate any structural differences, we superposed the RISC structure of AGO4 and the apo structure of *Nc*QDE2 C-lobe on their RNase H motifs within the PIWI domain (hereafter referred to as PIWI-catalytic subdomain) (Figure 3A). Notably, the rest of their PIWI domains encompassing α17 to the C terminus (hereafter referred to as PIWI-helical subdomain) are arranged differently, suggesting that the interaction between two PIWI subdomains differs in the absence of a guide strand. On the other hand, the MID domain and the PIWI-helical subdomain in the AGO4-RISC and apo-*Nc*QDE2 interact with each other quite similarly, involving similar conserved residues as well as their corresponding water molecules (Figure S4) (Boland et al., 2011). In apo-*Nc*QDE2, a sulfate ion occupying the interface between the MID domain and PIWI-helical subdomain seems to mimic a 5′ monophosphate of guide RNA, reinforcing their interaction (this will be further addressed later).

Our structural inspection of the guide-bound AGO4 and apo-*Nc*QDE2 C-lobe revealed a difference in the interface between their two PIWI subdomains. In the apo-*Nc*QDE2 C-lobe, the helical subdomain is tilted away from the β sheet of the PIWI-catalytic subdomain, and therefore there is a gap between the subdomains (Figure 3B, top). In contrast, the counterparts of the guide-bound AGO4 mesh in a shape-complementary manner (Figure 3B, middle). Note that the residues involved in the van der Waals interactions are conserved throughout eukaryotic AGOs (Figure S3). The same interactions are seen in the RISC structure of AGO2 (Figure 3B, bottom) (Schirle and MacRae, 2012) as well as AGO1 and AGO3 (Elkayam et al., 2012; Nakanishi et al., 2013; Park et al., 2017b). This structural difference between the presence and absence of guide RNA suggests that the bound guide RNA pushes the PIWI-helical subdomain toward the PIWI-catalytic subdomain during RISC assembly (Figure 3C). The current RISC structure shows that the seed region of guide RNA is recognized mainly by loop L4 of the PIWI-helical subdomain and loops $L3_1$ and $L3_2$ of the PIWI-catalytic subdomain, suggesting that the bound guide RNA ties the two PIWI subdomains together to form the composite PIWI domain.

Next, we tested the influence of this rearrangement of the two PIWI subdomains on the RISC assembly by inhibiting their shape-complementary interaction. For this purpose, we exploited the slicer enzyme activity of AGO2, whose RISC assembly is prerequisite for target cleavage. First, we expressed FLAG-AGO2 (Y529E), a well-known mutant deficient in duplex loading (Iwasaki et al., 2015a; Phan et al., 2018; Rüdel et al., 2011), in HEK293T cells and tested it for target cleavage. Like the catalytic mutant AGO2 (E637A), the Y529E mutant failed to cleave target RNA (Figure 3D), demonstrating the utility of this assay to evaluate the impact of a mutation on the RISC assembly. Then, G595 and V615 of AGO2 were mutated to isoleucine and alanine, respectively, to disrupt the shape-complementary interaction between the two PIWI subdomains. As a result, the double mutant completely lost its slicing activity (Figure 3D). To examine the impact of the mutations on duplex loading and passenger ejection, we performed the RISC maturation assay. AGO2 (E637A) loaded the small interfering RNA (siRNA) duplex and ejected the passenger strand as efficiently as did the WT (Figure 3E). In contrast, AGO2 (G595I/V615A) failed to load even a miR-20a duplex, like AGO2 (Y529E) (Figure 3E). This result suggests that the interaction between two PIWI subdomains is indispensable for loading of the small RNA duplex. These results support a molecular mechanism in which the bound guide RNA fastens the hydrophobic interface of the two PIWI subdomains.

It is well known that the glutamate finger is poised over the other three catalytic residues upon binding of guide RNA to complete the catalytic tetrad (Nakanishi et al., 2012). Catalytically active AGO2 and AGO3, as well as naturally slicer-deficient AGO1 and AGO4, have their fourth catalytic (or pseudo-catalytic) residue on α18, which is part of the PIWI-helical subdomain (Figure 3A) (Faehnle et al., 2013; Hauptmann et al., 2014; Liu et al., 2004; Meister et al., 2004; Nakanishi et al., 2013; Park et al., 2017b). Therefore, the conformational changes during RISC assembly rearrange two of the four catalytic (or pseudo-catalytic) residues.

Although loading of small RNAs increases the affinity of AGOs for TNRC6 proteins (Boland et al., 2011; Elkayam et al., 2017), little is known about the molecular mechanisms behind this. To investigate how formation of the composite PIWI domain affects binding to TNRC6 proteins, we expressed FLAG-AGO2, the E637A single mutant, or the G595I/V615A double mutant in HEK293T cells. Then, we tested if they are co-immunopurified with TNRC6A using an anti-FLAG antibody. The catalytic mutant, E637A, bound to TNRC6A comparably, whereas the double mutant drastically reduced its binding affinity (Figure 3F). This result suggests that the interaction between the two PIWI subdomains is prerequisite for the binding of TNRC6A.

(D) Target cleavage assay of AGO2 and mutants. The amount of AGOs used for target cleavage assays (right) was adjusted on the basis of the western blot with anti-FLAG antibody (left).

(E) Duplex loading of AGO2 and mutants. Black bars represent averages with independent replicates shown as dots. See also Figure S4E.

(F) Co-immunoprecipitation of TNRC6A with AGO2 and mutants. The amount of AGOs used to detect co-immunopurified TNRC6A with anti-TNRC6A antibody (right) was adjusted on the basis of the western blot with anti-FLAG antibody (left).

Experiments in (D) and (F) were performed at least three times. A representative gel is shown.

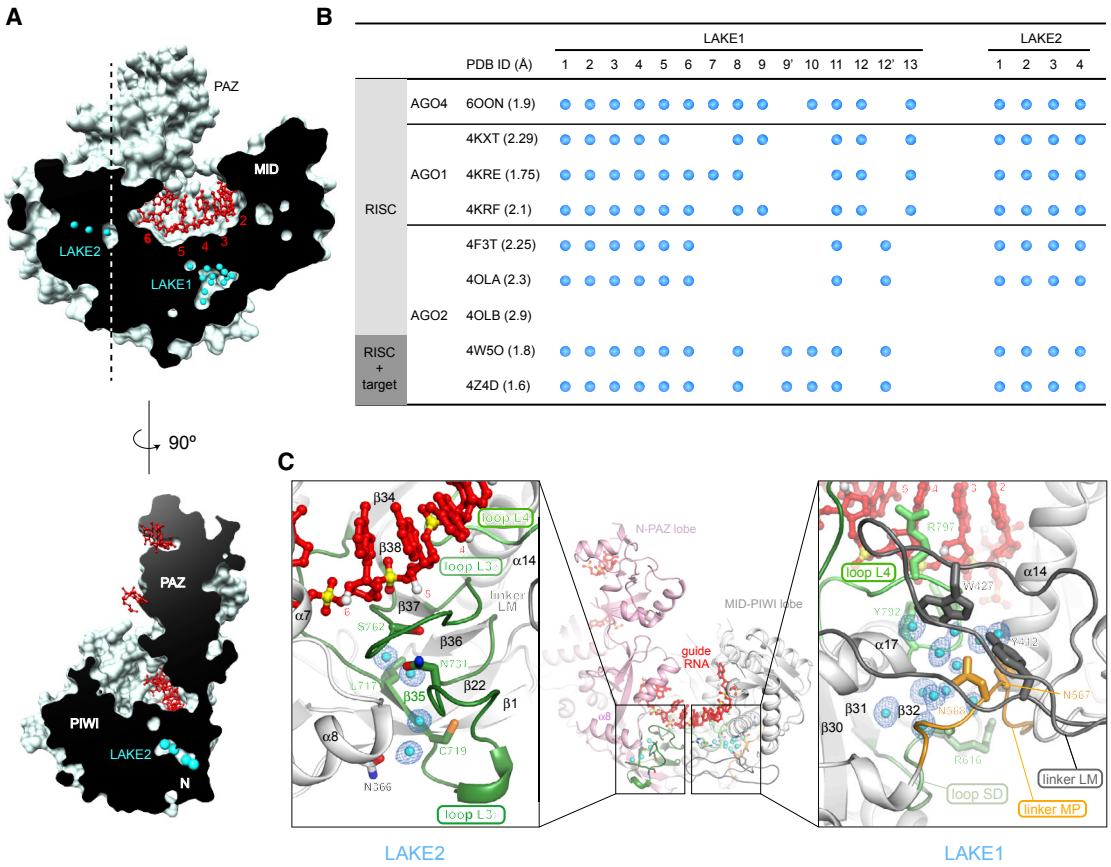

Figure 4. Two Water Clusters inside AGO4-RISC

(A) Cross sections of AGO4-RISC. Water molecules (cyan) are shown as spheres. The guide RNA (red) is displayed as a stick model.

(B) Conservation of internal water molecules among human AGOs. Water molecules equivalent to W9 and W12 in AGO4 have slightly different positions, W9′ and W12′, in AGO2, because of N623.

(C) Water molecules in LAKE1 (right) and LAKE2 (left). The simulated annealing F_o-F_c map (blue mesh) is contoured at 3.0 σ around the internal water molecules. See also Figures S5C and S5D.

Water Reservoirs inside AGO Proteins

Our 1.9 Å resolution crystal structure of AGO4 allowed us to identify two clusters of 13 and 4 water molecules, named LAKE1 and LAKE2 (loop-associated key estuary), respectively, located beneath the nucleic acid-binding channel (Figure 4A; Video S1). The water molecules that we located inside AGO4 are different from those previously found at the catalytic site (Schirle et al., 2014) and the target nucleotide-1 pocket (Schirle et al., 2015) (Figure S5A). At the LAKEs, all residues whose side chain participates in the hydrogen-bonding network with these water molecules are conserved throughout the four human AGOs, except that AGO2 has N623 instead of Ser (S615 in AGO4) (Figure S3). This finding suggests that the other human AGOs also accommodate water molecules in the same manner. Indeed, we observed water molecules at the corresponding positions in other available AGO-RISC structures, although the visibility of these water molecules varied depending on the resolution (Figure 4B) (Elkayam et al., 2012; Faehnle et al., 2013; Nakanishi et al., 2013; Schirle and MacRae, 2012; Schirle et al., 2014, 2015). The internal water clusters are seen also in the AGO2-RISC complex structure with a target RNA (PDB ID: 4Z4D) (Schirle et al., 2014), suggesting that LAKEs exist even after a guide-target duplex is propagated along the nucleic acid-binding channel.

The B-factors of water molecules in LAKEs (23–42 Å^2) are lower than the averaged B-factors of AGO4 protein atoms (Table 1), a hallmark of buried water molecules (Koellner et al., 2000). We investigated the crystallographic internal water molecules using ProACT2, a program that classifies water molecules on the basis of their solvent accessibility (Williams et al., 1994). All water molecules in LAKE1 and two in LAKE2 were categorized as buried water molecules that are completely sequestered from solvent (Figure S5B). Generally speaking, for soluble globular proteins, the hydrophobic effect is a major driving force of protein folding and excludes water molecules from the protein interior. Although sometimes a few water molecules are incorporated inside a folded structure to neutralize charged areas, they are isolated from each other (Carugo, 2016). In contrast, water molecules in the LAKEs form clusters. Therefore, it is unlikely that the observed 13 and 4 water molecules are trapped inside during the primary protein folding of AGO4.

LAKEs Are Not Pre-organized in Apo AGO

LAKE1 is located at the interfaces of three domains (L2, MID, and PIWI) where α14, α17, and four loops come together (Figure 4C, right). Two of the four loops are the domain linkers between L2 and MID domains (linker LM) and between MID and PIWI domains (linker MP). A previous study reported that apo-AGO2 was cleaved within these two domain linkers by thermolysin but became resistant after loading guide RNA (Elkayam et al., 2012). The third loop is loop L4 and is flexible in the absence of guide RNA, as seen in the apo structure of *Nc*QDE2 (Figure S4B) (Boland et al., 2011). Loop L4 uses one side to enclose 13 water molecules and the other side to interact with the guide nucleotide positions 2–5 (g2–g5) (Figure 4C, right). The fourth loop connecting β31 and β32 includes conserved serine (S) and aspartate (D) residues (hereafter, this loop is referred to as loop SD) (Figure 4C, right).

LAKE2 is formed by the helix-loop-helix motif (α7 and α8) of the L2 domain and loops $L3_1$ and $L3_2$ of the PIWI-catalytic subdomain (Figure 4C, left). Both loops are disordered in the absence of guide RNA (Boland et al., 2011), but fold into this unique shape once a guide RNA binds. Loops $L3_1$ and $L3_2$ recognize the phosphate backbone of g6–g8. Furthermore, loop $L3_2$ interacts with loop L4 and linker LM, directly or indirectly, via non-LAKE water molecules (Figure 4C, left). Thus, loops $L3_1$, $L3_2$, and L4 pave the composite nucleic acid-binding channel, suggesting that the LAKE formation is part of the RISC assembly process.

Domain Linkers and Loops Build LAKE1

As we have shown earlier (Figure 3B, middle), Y617 on loop SD and Y807 on α18 participate in van der Waals interactions between the two PIWI subdomains. These tyrosines also hydrogen bond with loop L4, directly or indirectly, via water molecules in LAKE1 (Figure 5A). As a result, the two tyrosine residues anchor loop SD and α18 to loop L4. To examine the influence of the tyrosine-centered interactions on RISC assembly, we replaced either of the corresponding tyrosines of AGO2 with alanine or phenylalanine, and the mutants were tested for target cleavage. The Y625A mutation (Y617 of AGO4) almost completely lost slicer activity, whereas the Y625F mutant retained comparable activity (Figure 5G), indicating that the aromatic ring of Y625, not the hydroxyl group, is essential for RISC assembly. Supporting this, the hydroxyl group of Y625 interacts with T789 (T791 in AGO4) via a water molecule, W3 (Figures 5A and 5D), but the T789V mutation did not affect slicer activity (Figure 5G). Even the double mutant of Y625F/T789V showed comparable activity with the WT (Figure 5G). In contrast, Y805A and Y805F (Y807 of AGO4) drastically decreased the slicer activity (Figure 5G), indicating that both the hydroxyl group and aromatic ring of Y805 are critical for RISC assembly.

In AGO4-RISC, W427 on linker LM is stacked with T796 on loop L4 while Y412 on linker LM hydrogen-bonds with N568 on linker MP (Figure 5B). These interactions anchor both loop L4 and linker MP to linker LM. When the corresponding tryptophan (W435) of AGO2 (Figure 5E) was mutated to alanine, the mutation drastically decreased slicer activity (Figure 5G). On the other hand, alanine mutations of Y420 (Y412 of AGO4) and N576 (N568 of AGO4) reduced slicer activity to about half that of the WT (Figure 5G). These results suggest the significance of these residues for RISC assembly.

The current AGO4 structure has shown that N567 on linker MP hydrogen-bonds with the side chain of N560 and the carbonyl oxygen of L557, both of which are located on α14 of the MID domain (Figures 5B and S6C). The same interactions are seen in AGO2-RISC (PDB ID: 4OLA) (Figure 5E), but not in the previously reported crystal structure of an isolated AGO2 MID domain that has no interaction with the flanking linkers LM and MP (Figures S6D and S6E) (Frank et al., 2010). This difference suggests that linkers LM and MP are free to move until they form LAKE1 with loop L4 upon binding of guide RNA. To investigate the influence of the asparagine-centered interactions on RISC assembly, single-point mutants of N568 and N575 of AGO2 (N560 and N567 of AGO4, respectively) were tested for target cleavage. Both alanine mutations diminished slicer activity (Figure 5G).

Our structural observation indicates that the L2 and MID domains and two PIWI subdomains converge to form LAKE1 through the interactions of the two loops (L4 and SD), two linkers (LM and MP) and two helices (α14 and α18). Because LAKE1 is located far from the catalytic site, it seemed unlikely that the replacement of even a single residue forming LAKE1 directly affected the target cleavage. Rather, it would be plausible that the single mutations had a negative impact on duplex loading or passenger ejection, thereby lowering the target cleavage activity. To validate this idea, all AGO2 mutants that poorly cleaved target RNAs in Figure 5G were tested for RISC assembly. The results showed that most of these mutants failed to load duplexes (Figure 5H). However, once loaded with a duplex, those mutants efficiently ejected the passenger strand to become the mature RISC (Figure 5I), suggesting that LAKE1 needs to be established prior to passenger ejection. Last, to see whether LAKE1 formation is also essential for AGO4 to load duplexes, we made three single mutations, N560A, N567A, and Y807F, on AGO4, which correspond to N568A, N575A, and Y805F on AGO2, respectively, and tested them for RISC maturation. These AGO4 mutants failed to load duplexes (Figure 5J). Altogether, these results demonstrate the significance of LAKE formation for the duplex-loading step.

Confined LAKE Water Molecules Are Exchangeable

To investigate the dynamics of the LAKE water molecules, we performed all-atom MD simulations of AGO4 and AGO2 keeping all crystallographic water molecules in their initial positions. The simulations performed at 300 and 310 K revealed that the occupancy of LAKE1 fluctuated, yet no dehydration was observed in the simulated timescale (~100 ns) (Figures 6A and 6B). This result indicates that water molecules are confined inside the cavity but are continuously exchanged with the bulk solvent. The exchange rate can be quantified by estimating the survival probability $P(\tau)$ (i.e., the probability of a water molecule to remain inside the cavity after a certain amount of time). As shown in Figure 6C, the decay in $P(\tau)$ for water molecules in LAKE1 is slower than the bulk, and determination of a decay rate required a biexponential fit of the $P(\tau)$ curve with a fast and a slow decay constant (Table S1). This further suggests that water is highly confined inside LAKE1 and that water molecules in different regions of LAKE1 may experience different degrees of confinement given by geometry and/or favorable interactions. Interestingly, although AGO4 shows a greater number of water molecules in the crystallographic structure (13 versus 8–10 from

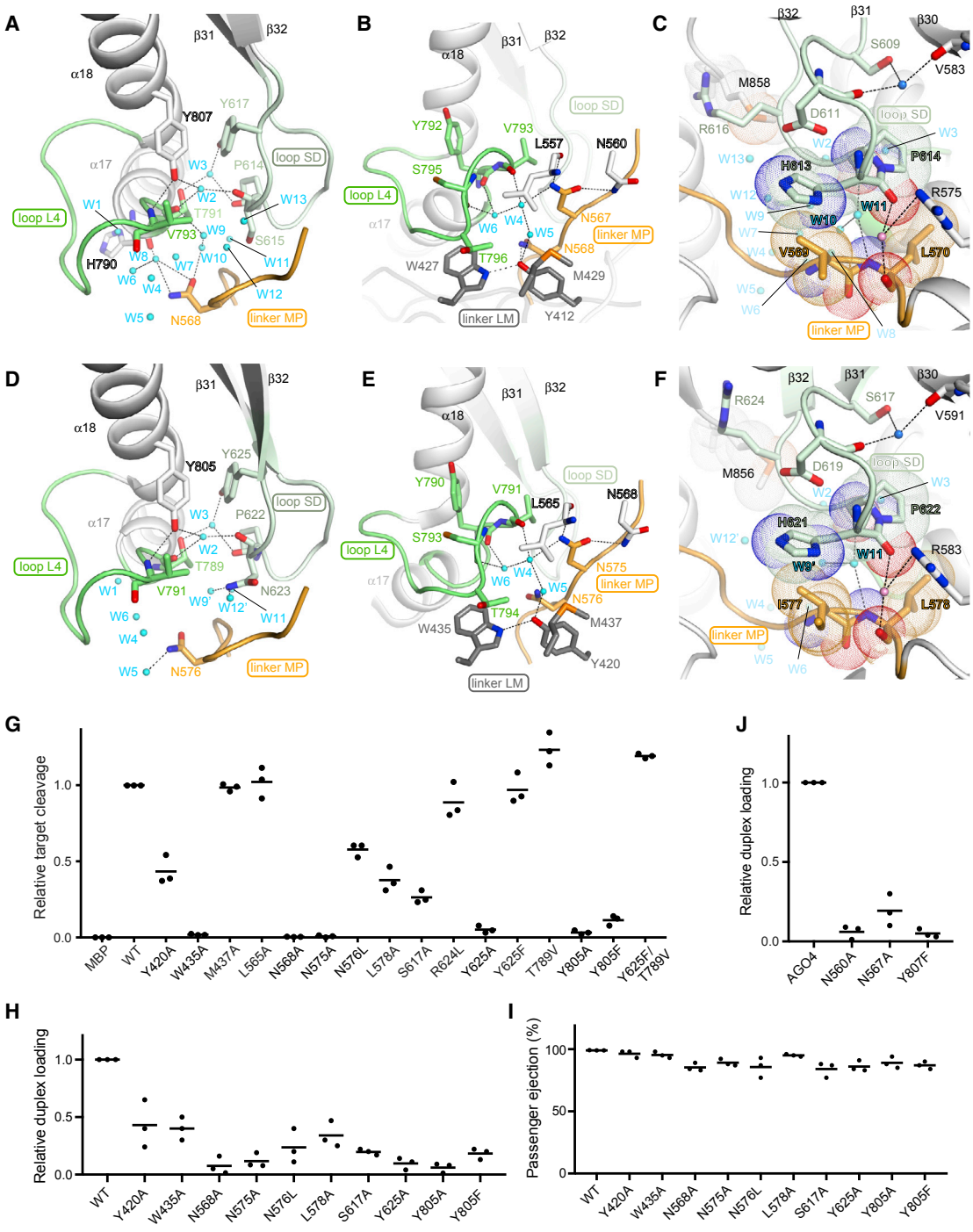

Figure 5. Water-Mediated Hydrogen-Bonding Network of LAKE1

(A–F) AGO4 LAKE1 (top row) and AGO2 LAKE1 (bottom row) involving their conserved residues in water-mediated interactions among α18, linker MP, and loops L4 and SD (A and D), among linkers LM and MP, and loop L4 (B and E), and between linker MP and loop SD (C and F). Colors as in Figure 4C. Water molecules (cyan) and hydrogen bonds are depicted as spheres and dotted lines, respectively.

(G) Target cleavage assays with AGO2 and mutants. See also Figures S6A–S6C.

(H and I) Duplex loading (H) and passenger ejection (I) of AGO2 mutants that drastically reduced their target cleavage in (G). See also Figure S6F.

(J) Duplex loading of AGO4 mutants. See also Figure S6G.

Black bars in (G)–(J) represent averages with independent replicates shown as dots.

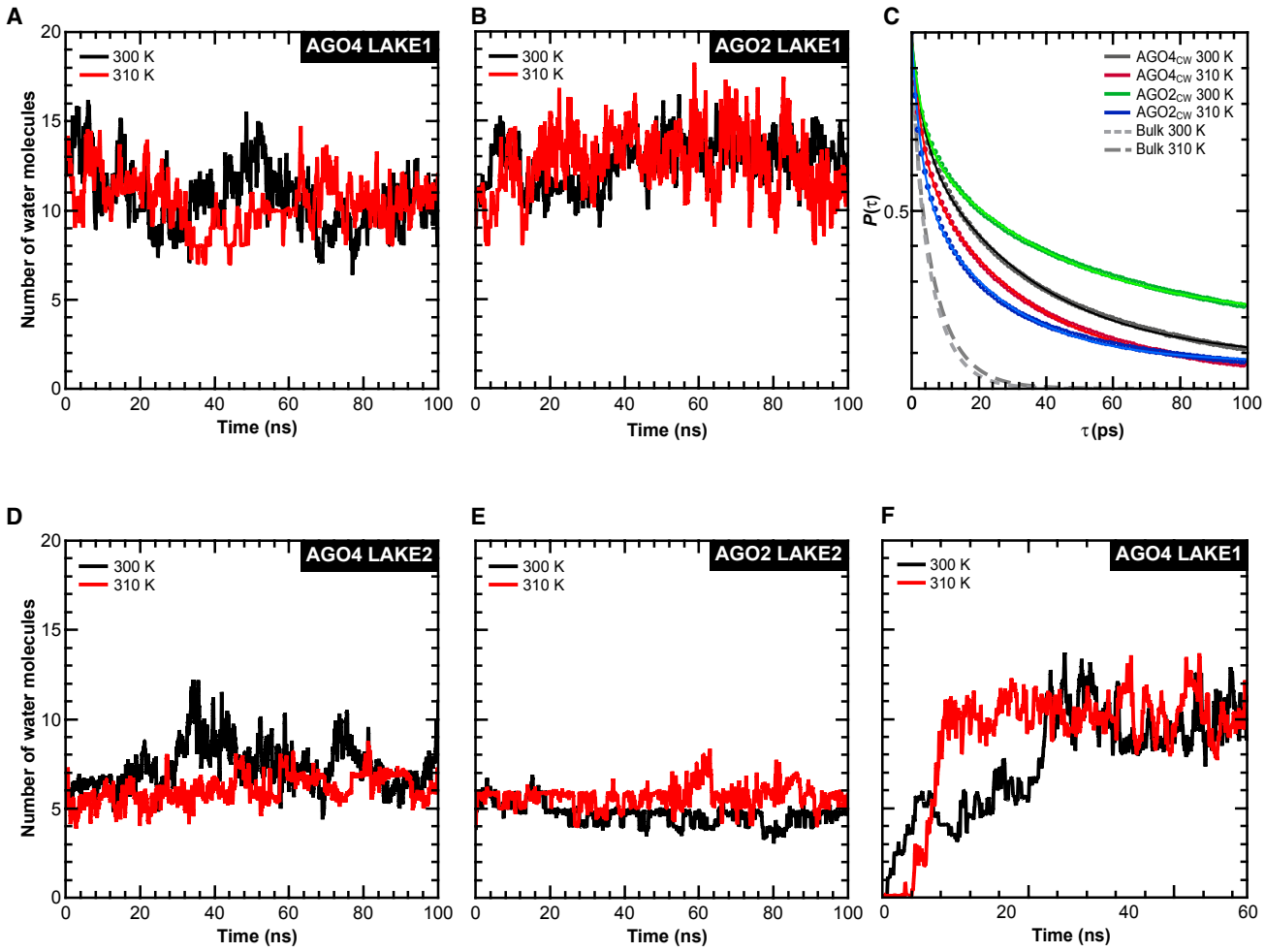

Figure 6. Dynamic Behavior of Simulated Water Molecules in LAKE1 and LAKE2

(A, B, D, and E) Water occupancy versus time in LAKE1 of AGO4 (A) and AGO2 (B) and in LAKE 2 of AGO4 (D) and AGO2 (E) simulated with crystallographic water molecules in their initial positions ($AGO4_{CW}$, $AGO2_{CW}$) at 300 K (black) and 310 K (red).

(C) Survival probability $P(\tau)$ for water molecules inside LAKE1 of $AGO4_{CW}$ and $AGO2_{CW}$ simulated at 300 and 310 K. Solid and dotted lines correspond to biexponential fits to the AGO4 and AGO2 data and to exponential fits to the bulk data, respectively (Table S1).

(F) Water occupancy versus time in LAKE1 of AGO4 simulated without crystallographic water molecules at the start of the simulation ($AGO4_{NCW}$) at 300 K (black) and 310 K (red).

Lines in (A), (B), and (D)–(F) correspond to 100 ps moving window averages.

AGO2), this trend is reversed during the simulations (average occupancy of AGO4 10 ± 2 versus AGO2 13 ± 1; Table S1).

Structures of both AGO2 and AGO4 have four crystallographic water molecules inside LAKE2 (Figure 4C, left) and an average of about six water molecules during the simulations (Figures 6D and 6E). The analysis of LAKE2 dynamics for AGO4 showed a marked increase in occupancy of the cavity at $t_{sim} \sim 30$ ns. Visual inspection of the trajectory of AGO4 at 300 K revealed that the interaction between loops $L3_1$ and $L3_2$ was transiently disrupted, thereby allowing more water molecules to enter LAKE2. Subsequently, the conformation was partially reverted while the water occupancy remained high until $t_{sim} \sim 60$ ns.

These simulation predictions suggest that internal water molecules in LAKEs are confined but move and are exchangeable with solvent.

LAKE Water Molecules Maintain the Composite RISC

Most of the conserved residues on the domain linkers and loops around LAKE1 directly interact with the internal water molecules (Figure S6C). This observation prompted us to raise the hypothesis that water molecules in LAKEs offer an adhesive property to maintain the domain-domain interactions within the mature RISC. Supporting this, single mutations of the corresponding conserved residues of AGO2 severely affected the RISC assembly and thus slicing activity (Figures 5G–5I). Meanwhile, using their non-polar side chains, M429 and L557 form part of the interior wall of LAKE1 (Figure 5B), but mutants of their corresponding residues in AGO2, M437A and L565A, retained a comparable slicing activity with WT (Figures 5E and 5G). These results indicate that internal water molecules are recognized by hydrogen bonds, consistent with our MD simulations in which water

molecules transfer from one place to another within LAKE1, but always occupy specific positions rather than randomly moving around (Video S2). To validate our hypothesis that RISCs proactively incorporate solvent water molecules into the cavity to stabilize the composite structure, we started MD simulations in an initial state in which the crystallographic water molecules were removed from AGO4 LAKE1. Immediately after simulations start, solvent water molecules filled the cavity (Figure 6F), which is strong evidence that the uptake of water molecules into AGO4 is energetically preferable. These results suggest that the water-mediated hydrogen-bonding network stabilizes the composite RISC.

MD trajectories also showed two gates through which water molecules enter and exit the AGO4 LAKE1 (Figures 5C and S6I). The first of these (gate 1), is composed of M610 and R616 on loop SD and H856 and M858 on the C-terminal loop. Our MD analysis indicated that R616 located at the edge of gate 1 seemed to control the rate of entry and exit of water molecules. To investigate the significance of this arginine residue, we mutated the corresponding R624 of AGO2 to leucine (Figure 5F). The mutant retained a comparable activity (Figure 5G), suggesting that the flow rate of water molecules does not affect the function of RISC. The second gate (gate 2) is formed by V569 and L570 on linker MP and H613 and P614 on loop SD (Figures 5C and S6I). When L578 of AGO2, corresponding to L570 of AGO4, was mutated to alanine, the slicer activity was reduced to less than half that of the WT (Figure 5G). Residue S609 forms tripartite hydrogen bonds, which uniquely kink loop SD, and thus shapes the two gates (Figure 5C). An AGO2 alanine mutant of the corresponding residue, S617, largely decreased the slicer activity (Figures 5F and 5G). In our RISC maturation assay, both L578A and S617A mutations drastically affected duplex loading of AGO2 (Figure 5H). These results suggest that a fully functional RISC needs to shape these two gates properly.

DISCUSSION

In this study, our combined approach revealed that the seed region of guide RNA ties together the two PIWI subdomains, forming the composite PIWI domain and two LAKEs. These data provide the following insights.

Update of RISC Loading Mechanism

A previously reported crystal structure of *Thermus thermophilus* AGO (PBD ID: 3DLB) (Wang et al., 2008) captured a state in which the 10 nt guide strand was recognized at its 3′ end by the PAZ domain, but its length was too short to reach the 5′ monophosphate-binding site on the MID domain. As a result, the PIWI-helical subdomain was completely disordered, while the apo MID domain directly interacted with the PIWI-catalytic subdomain (Video S3). This conformation was not well understood, but now it can be explained by considering the existence of two PIWI subdomains that are free to move independently unless they are tied by the seed region of the guide strand. In support of this, the crystal structure of apo-*Nc*QDE2 C-lobe showed a loose interaction between the two PIWI subdomains because of the absence of a guide RNA (Boland et al., 2011). Nevertheless, the PIWI-helical subdomain tightly interacts with the MID domain, as do the counterparts of AGO4-RISC (Video S3). Given that in the *Nc*QDE2 C-lobe, a sulfate ion is recognized at the 5′ monophosphate-binding site between the MID domain and PIWI-helical subdomain, binding of the 5′ monophosphate of the guide strand may reinforce their interaction.

On the basis of our data and previous studies, we propose here a model of RISC loading (Video S4). Loops L4 and SD and linkers LM and MP would be solvent exposed and flexible prior to the binding of guide RNA, which allows the MID domain and two PIWI subdomains to move independently. Then, the MID domain and PIWI-helical subdomain capture a 5′ monophosphate of the duplex and flip out the base of g1. The resultant ternary complex would last longer if the first nucleotide base is adenine or uracil, because of the high affinity of the MID domain for those bases (Frank et al., 2010). Subsequently, loop L4 and α18 of the PIWI-helical subdomain recognize the phosphate backbone of g2–g5 and load the duplex to the rest of AGO, such that loops $L3_1$ and $L3_2$ recognize the g6–g8. As a result, the two PIWI subdomains are tied together by the seed region (g2–g8). Before binding to a duplex, the MID domain and the PIWI subdomains solvent-expose their hydrophobic interfaces, providing good clients for the heat shock proteins (HSPs) that are required for sufficient RISC loading (Iki et al., 2010; Iwasaki et al., 2010, 2015a). Because binding of a duplex occludes the hydrophobic areas, HSPs would then be released and no longer involved in the subsequent passenger ejection step, which could explain a previous report that HSPs are essential only for the duplex-loading step (Iwasaki et al., 2010).

PIWI Proteins Have No LAKEs

Like AGOs, PIWI proteins (PIWIs), together with PIWI-interacting RNAs (piRNAs), form piRNA-induced silencing complexes (piRISCs) (Czech and Hannon, 2016; Ghildiyal and Zamore, 2009; Iwasaki et al., 2015b). To see whether piRISCs also possess internal water molecules, we investigated the previously determined crystal structure of piRNA-bound silkworm PIWI protein, Siwi (Matsumoto et al., 2016). Siwi replaces the residues corresponding to N568, T791, and V793 of AGO4 with tryptophan (W655), leucine (L856), and phenylalanine (F858), respectively (Figures 7A and 7B). These bulky, non-polar residues occupy the space where the internal water molecules are found in AGO4. As a result, Siwi-piRISC has only two internal water molecules corresponding to W1 and W3 of AGO4 LAKE1 (Figure 7B). The two buried water molecules are isolated from each other, like those trapped during the primary protein folding. In addition, Siwi substitutes non-polar residues for the polar ones that recognize the internal water molecules in AGO4 LAKE2 (Figures 7C and 7D). Accordingly, Siwi-piRISC forms a tightly packed hydrophobic core without the aid of internal water molecules. Notably, the aforementioned hydrophobic residues are conserved throughout PIWIs (Figure S7), suggesting that other PIWIs also assemble into piRISC without LAKEs. This discrepancy between AGOs and PIWIs may reflect the differences in their RISC assemblies. The nucleic acid-binding channel of eukaryotic AGOs is not wide enough to load a duplex, suggesting that drastic conformational changes are essential for duplex loading. In contrast, PIWIs incorporate single-stranded

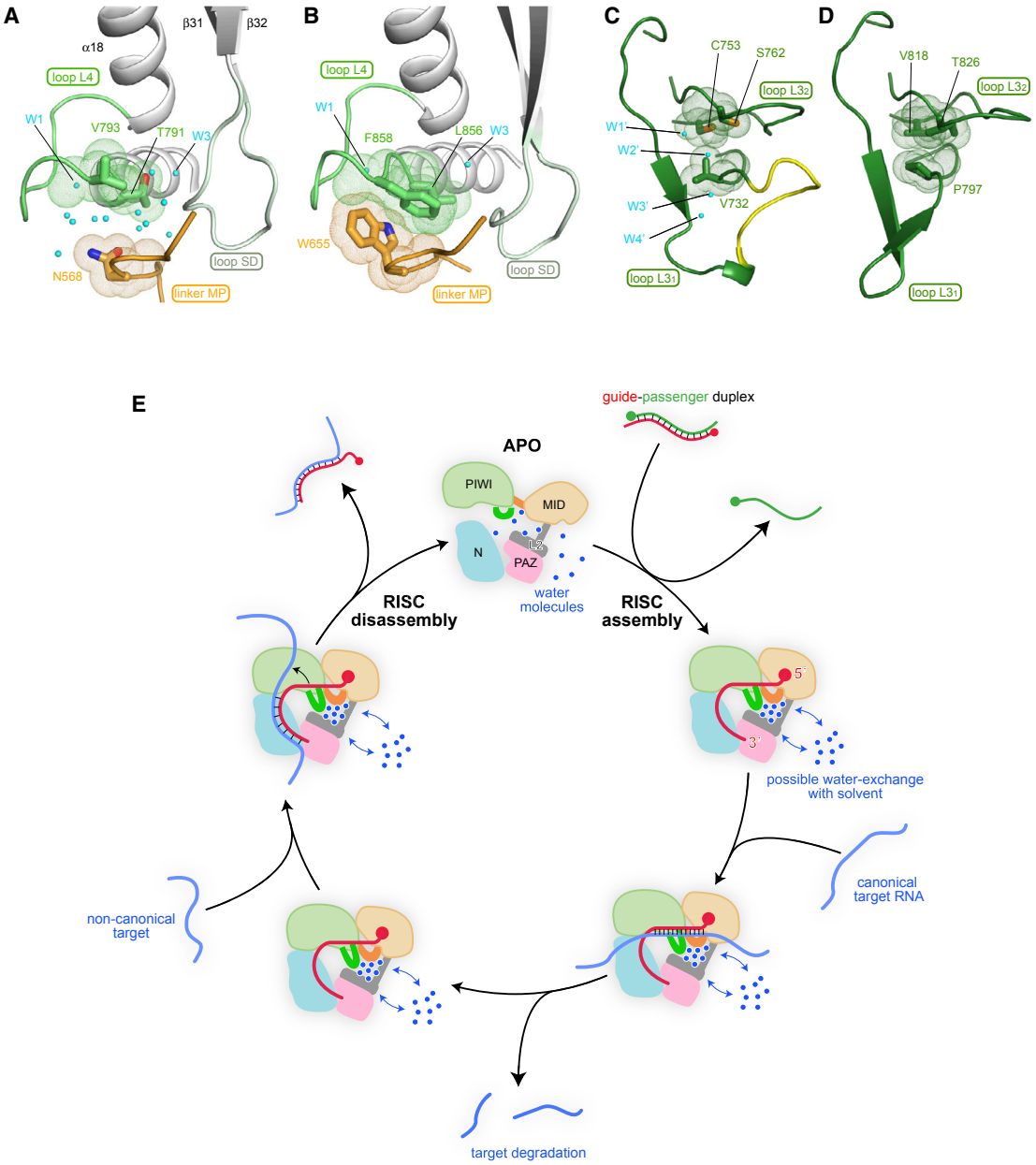

Figure 7. AGOs, but Not PIWIs, Possess LAKEs

(A and B) Interactions between loop L4 and linker MP in AGO4 (A) and Siwi (B) (PDB ID: 5GUH). The van der Waals surfaces are shown as dots.

(C and D) Interactions of loops $L3_1$ and $L3_2$ in AGO4 (C) and Siwi (D). The AGO-specific insert (yellow) makes space for four water molecules (LAKE2).

(E) Model of the water-mediated RISC assembly and disassembly (see the main text for details). The MD simulation predicts that mature RISC exchanges water molecules in LAKEs with the solvent (blue arrows). The water-mediated RISC disassembly is hypothetical on the basis of our and previous studies.

precursor piRNAs. Therefore, apo PIWIs may pre-organize the composite nucleic acid-binding channel and thereby may not require a large conformational change for piRISC assembly.

The possession of LAKEs may also reflect the difference in the turnover mechanisms between AGOs and PIWIs. It is well known that AGOs are expressed ubiquitously in different cells (Farazi et al., 2008; Meister et al., 2004; Sasaki et al., 2003) and that the half-life of RISCs is on the order of days to weeks (De et al., 2013). Therefore, AGOs have many opportunities to exchange guide RNAs. Supporting this idea, the MacRae group reported that highly complementary target RNAs promote the release of guide RNAs from human AGO2 (De et al., 2013). A subsequent detailed study by the Shin group revealed that loaded guide RNAs can be released by hybridization with non-canonical target RNAs that are fully complementary to the guide except for its 5′ nucleotides (Park et al., 2017a). These studies demonstrate

that AGOs can unload guide RNAs. Although the molecular mechanism remains elusive, it can be imagined that topological stress is accumulated on the seed region (g2–g8) as the guide-non-canonical target duplex is propagated toward the 5′ end of the guide strand. In this study, we have revealed that internal water molecules connect the L2 and MID domains along with the PIWI subdomains through their water-mediated hydrogen bonds. In addition, our MD simulations predict that internal water molecules move, indicating that their hydrogen bonds are transiently broken without disrupting the conformation of the RISC. Although direct experimental validation of these predictions is yet to come, our functional analyses are consistent with all simulation results. Therefore, we hypothesize that the transient rupture of water-mediated loop-loop interactions would enable the RISCs to collapse when the topological stress reaches a threshold (Figure 7E). In contrast, PIWIs stabilize their piRISC conformation by forming a hydrophobic core without LAKEs (Matsumoto et al., 2016). Such tight hydrophobic interactions would make piRISC difficult to disassemble. Given that PIWI proteins are predominantly expressed in germ cells only during a short term (Farazi et al., 2008), they do not seem to have enough time to exchange piRNAs, if any, and their exchange efficiency may be much lower than that of AGOs. These properties could explain why piRISCs do not incorporate internal water molecules.

Internal water molecules have been identified in high-resolution structures (Meyer, 1992; Park and Saven, 2005). Functional studies and MD simulations have revealed that trapped water molecules contribute to the structural stability and affinity for ligands (Ball, 2017; Levy and Onuchic, 2006; Park and Saven, 2005). A recent structural study of GPCR reported that the internal water molecules work as a ''lubricating oil'' for the movement of a transmembrane helix (Yuan et al., 2014). In the present study, we discovered the significance of the internal water molecules for RISC assembly and discussed their possible involvement in RISC disassembly. Our simulation predictions and functional assays suggest another property of internal water molecules, one that facilitates a drastic, yet reversible, conformational change of globular proteins comprising multi-domains.

STAR★METHODS

Detailed methods are provided in the online version of this paper and include the following:

- KEY RESOURCES TABLE
- LEAD CONTACT AND MATERIALS AVAILABILITY
- EXPERIMENTAL MODEL AND SUBJECT DETAILS
- METHOD DETAILS
  - Cloning, expression, and purification of AGO proteins and TNRC6B fragments
  - Crystallization, structure determination and refinement
  - Cell culture, transfection, cell lysis and western blot
  - *In vitro* cleavage assay
  - RISC maturation assay
  - Filter binding assay
  - Binding assay with TNRC6 fragments
  - Simulation systems preparation
  - MD simulations
  - Definition of LAKE1 and LAKE2 for estimation of water dynamics parameters from the MD trajectories
  - Computation of survival probability of water molecules in MD simulations
- QUANTIFICATION AND STATISTICAL ANALYSIS
- DATA AND CODE AVAILABILITY

SUPPLEMENTAL INFORMATION

Supplemental Information can be found online at https://doi.org/10.1016/j.molcel.2019.06.011.

ACKNOWLEDGMENTS

We are grateful to K. Okamura (Nara Institute of Science and Technology [NAIST]) for useful advice and insights. This work was supported by Pelotonia Fellowships (to M.S.P., R.A.-S., and D.M.D.), The Ohio State University startup funds (to M.S. and K.N.), PRESTO (grant JPMJPR13L7 to K.N.), and the NIH (grants R01GM124320 to K.N. and R01DC015271 to M.S.). The research was supported by the Office of the Director, NIH (grant S10OD023582). This work is based upon research conducted at the Northeastern Collaborative Access Team beamlines, which are funded by the National Institute of General Medical Sciences of the NIH (grant P41 GM103403). The Eiger 16M detector on 24-ID-E beamline is funded by a NIH Office of Research Infrastructure Programs (ORIP) HEI grant (S10OD021527). This research used resources of the Advanced Photon Source, a U.S. Department of Energy (DOE) Office of Science User Facility operated for the DOE Office of Science by Argonne National Laboratory under contract DE-AC02-06CH11357. All MD simulations were carried out at the Ohio Supercomputer Center using the Owens cluster (grant PAS1037 to M.S.).

AUTHOR CONTRIBUTIONS

J.A.B. expressed, purified, and crystallized human AGO4. J.A.B., D.M.D., and K.N. collected the x-ray diffraction dataset. K.N. determined the crystal structure. M.S.P., A.C.K., H.-D.P., and E.W. performed functional analyses. R.A.-S. and M.S. performed and analyzed the MD simulations. K.N. supervised the project and wrote the manuscript. All authors edited the manuscript.

DECLARATION OF INTERESTS

The authors declare no competing interests.

Received: November 19, 2018
Revised: April 30, 2019
Accepted: June 7, 2019
Published: July 16, 2019

REFERENCES

Adams, P.D., Afonine, P.V., Bunkóczi, G., Chen, V.B., Davis, I.W., Echols, N., Headd, J.J., Hung, L.W., Kapral, G.J., Grosse-Kunstleve, R.W., et al. (2010). PHENIX: a comprehensive Python-based system for macromolecular structure solution. Acta Crystallogr. D Biol. Crystallogr. *66*, 213–221.

Alló, M., Agirre, E., Bessonov, S., Bertucci, P., Gómez Acuña, L., Buggiano, V., Bellora, N., Singh, B., Petrillo, E., Blaustein, M., et al. (2014). Argonaute-1 binds transcriptional enhancers and controls constitutive and alternative splicing in human cells. Proc. Natl. Acad. Sci. U S A *111*, 15622–15629.

Araya-Secchi, R., Perez-Acle, T., Kang, S.G., Huynh, T., Bernardin, A., Escalona, Y., Garate, J.A., Martínez, A.D., García, I.E., Sáez, J.C., and Zhou, R. (2014). Characterization of a novel water pocket inside the human Cx26 hemichannel structure. Biophys. J. *107*, 599–612.

Azuma-Mukai, A., Oguri, H., Mituyama, T., Qian, Z.R., Asai, K., Siomi, H., and Siomi, M.C. (2008). Characterization of endogenous human Argonautes and

their miRNA partners in RNA silencing. Proc. Natl. Acad. Sci. U S A *105*, 7964–7969.

Baillat, D., and Shiekhattar, R. (2009). Functional dissection of the human TNRC6 (GW182-related) family of proteins. Mol. Cell. Biol. *29*, 4144–4155.

Ball, P. (2017). Water is an active matrix of life for cell and molecular biology. Proc. Natl. Acad. Sci. U S A *114*, 13327–13335.

Bartel, D.P. (2018). Metazoan microRNAs. Cell *173*, 20–51.

Battye, T.G., Kontogiannis, L., Johnson, O., Powell, H.R., and Leslie, A.G. (2011). iMOSFLM: a new graphical interface for diffraction-image processing with MOSFLM. Acta Crystallogr. D Biol. Crystallogr. *67*, 271–281.

Beitzinger, M., Peters, L., Zhu, J.Y., Kremmer, E., and Meister, G. (2007). Identification of human microRNA targets from isolated argonaute protein complexes. RNA Biol. *4*, 76–84.

Bernstein, E., Caudy, A.A., Hammond, S.M., and Hannon, G.J. (2001). Role for a bidentate ribonuclease in the initiation step of RNA interference. Nature *409*, 363–366.

Boland, A., Huntzinger, E., Schmidt, S., Izaurralde, E., and Weichenrieder, O. (2011). Crystal structure of the MID-PIWI lobe of a eukaryotic Argonaute protein. Proc. Natl. Acad. Sci. U S A *108*, 10466–10471.

Carugo, O. (2016). Statistical survey of the buried waters in the Protein Data Bank. Amino Acids *48*, 193–202.

Cheloufi, S., Dos Santos, C.O., Chong, M.M., and Hannon, G.J. (2010). A dicer-independent miRNA biogenesis pathway that requires Ago catalysis. Nature *465*, 584–589.

Czech, B., and Hannon, G.J. (2016). One loop to rule them all: the ping-pong cycle and piRNA-guided silencing. Trends Biochem. Sci. *41*, 324–337.

Dayeh, D.M., Kruithoff, B.C., and Nakanishi, K. (2018). Structural and functional analyses reveal the contributions of the C- and N-lobes of Argonaute protein to selectivity of RNA target cleavage. J. Biol. Chem. *293*, 6308–6325.

De, N., Young, L., Lau, P.W., Meisner, N.C., Morrissey, D.V., and MacRae, I.J. (2013). Highly complementary target RNAs promote release of guide RNAs from human Argonaute2. Mol. Cell *50*, 344–355.

Dueck, A., Ziegler, C., Eichner, A., Berezikov, E., and Meister, G. (2012). microRNAs associated with the different human Argonaute proteins. Nucleic Acids Res. *40*, 9850–9862.

Elkayam, E., Kuhn, C.D., Tocilj, A., Haase, A.D., Greene, E.M., Hannon, G.J., and Joshua-Tor, L. (2012). The structure of human argonaute-2 in complex with miR-20a. Cell *150*, 100–110.

Elkayam, E., Faehnle, C.R., Morales, M., Sun, J., Li, H., and Joshua-Tor, L. (2017). Multivalent recruitment of human Argonaute by GW182. Mol. Cell *67*, 646–658.e3.

Faehnle, C.R., Elkayam, E., Haase, A.D., Hannon, G.J., and Joshua-Tor, L. (2013). The making of a slicer: activation of human Argonaute-1. Cell Rep. *3*, 1901–1909.

Farazi, T.A., Juranek, S.A., and Tuschl, T. (2008). The growing catalog of small RNAs and their association with distinct Argonaute/Piwi family members. Development *135*, 1201–1214.

Fire, A., Xu, S., Montgomery, M.K., Kostas, S.A., Driver, S.E., and Mello, C.C. (1998). Potent and specific genetic interference by double-stranded RNA in Caenorhabditis elegans. Nature *391*, 806–811.

Frank, F., Sonenberg, N., and Nagar, B. (2010). Structural basis for 5′-nucleotide base-specific recognition of guide RNA by human AGO2. Nature *465*, 818–822.

Ghildiyal, M., and Zamore, P.D. (2009). Small silencing RNAs: an expanding universe. Nat. Rev. Genet. *10*, 94–108.

Gowers, R.J., Linke, M., Barnoud, J., Reddy, T.J.E., Melo, M.N., Seyler, S.L., Domanski, J., Dotson, D.L., Buchoux, S., Kenney, I.M., et al. (2016). MDAnalysis: a Python package for the rapid analysis of molecular dynamics simulations. In Proceedings of the 15th Python in Science Conference, S. Benthall and S. Rostrup, eds., pp. 98–105.

Gregory, R.I., Chendrimada, T.P., Cooch, N., and Shiekhattar, R. (2005). Human RISC couples microRNA biogenesis and posttranscriptional gene silencing. Cell *123*, 631–640.

Hafner, M., Landthaler, M., Burger, L., Khorshid, M., Hausser, J., Berninger, P., Rothballer, A., Ascano, M., Jr., Jungkamp, A.C., Munschauer, M., et al. (2010). Transcriptome-wide identification of RNA-binding protein and microRNA target sites by PAR-CLIP. Cell *141*, 129–141.

Hauptmann, J., Dueck, A., Harlander, S., Pfaff, J., Merkl, R., and Meister, G. (2013). Turning catalytically inactive human Argonaute proteins into active slicer enzymes. Nat. Struct. Mol. Biol. *20*, 814–817.

Hauptmann, J., Kater, L., Löffler, P., Merkl, R., and Meister, G. (2014). Generation of catalytic human Ago4 identifies structural elements important for RNA cleavage. RNA *20*, 1532–1538.

Hauptmann, J., Schraivogel, D., Bruckmann, A., Manickavel, S., Jakob, L., Eichner, N., Pfaff, J., Urban, M., Sprunck, S., Hafner, M., et al. (2015). Biochemical isolation of Argonaute protein complexes by Ago-APP. Proc. Natl. Acad. Sci. U S A *112*, 11841–11845.

Haussecker, D., Cao, D., Huang, Y., Parameswaran, P., Fire, A.Z., and Kay, M.A. (2008). Capped small RNAs and MOV10 in human hepatitis delta virus replication. Nat. Struct. Mol. Biol. *15*, 714–721.

Hu, Q., Tanasa, B., Trabucchi, M., Li, W., Zhang, J., Ohgi, K.A., Rose, D.W., Glass, C.K., and Rosenfeld, M.G. (2012). DICER- and AGO3-dependent generation of retinoic acid-induced DR2 Alu RNAs regulates human stem cell proliferation. Nat. Struct. Mol. Biol. *19*, 1168–1175.

Huang, J., and MacKerell, A.D., Jr. (2013). CHARMM36 all-atom additive protein force field: validation based on comparison to NMR data. J. Comput. Chem. *34*, 2135–2145.

Huang, V., Zheng, J., Qi, Z., Wang, J., Place, R.F., Yu, J., Li, H., and Li, L.C. (2013). Ago1 Interacts with RNA polymerase II and binds to the promoters of actively transcribed genes in human cancer cells. PLoS Genet. *9*, e1003821.

Humphrey, W., Dalke, A., and Schulten, K. (1996). VMD: visual molecular dynamics. J. Mol. Graph. *14*, 33–38, 27–38.

Huntzinger, E., and Izaurralde, E. (2011). Gene silencing by microRNAs: contributions of translational repression and mRNA decay. Nat. Rev. Genet. *12*, 99–110.

Iki, T., Yoshikawa, M., Nishikiori, M., Jaudal, M.C., Matsumoto-Yokoyama, E., Mitsuhara, I., Meshi, T., and Ishikawa, M. (2010). In vitro assembly of plant RNA-induced silencing complexes facilitated by molecular chaperone HSP90. Mol. Cell *39*, 282–291.

Iwasaki, S., and Tomari, Y. (2018). Reconstitution of RNA interference machinery. Methods Mol. Biol. *1680*, 131–143.

Iwasaki, S., Kobayashi, M., Yoda, M., Sakaguchi, Y., Katsuma, S., Suzuki, T., and Tomari, Y. (2010). Hsc70/Hsp90 chaperone machinery mediates ATP-dependent RISC loading of small RNA duplexes. Mol. Cell *39*, 292–299.

Iwasaki, S., Sasaki, H.M., Sakaguchi, Y., Suzuki, T., Tadakuma, H., and Tomari, Y. (2015a). Defining fundamental steps in the assembly of the Drosophila RNAi enzyme complex. Nature *521*, 533–536.

Iwasaki, Y.W., Siomi, M.C., and Siomi, H. (2015b). PIWI-interacting RNA: its biogenesis and functions. Annu. Rev. Biochem. *84*, 405–433.

Jakymiw, A., Lian, S., Eystathioy, T., Li, S., Satoh, M., Hamel, J.C., Fritzler, M.J., and Chan, E.K. (2005). Disruption of GW bodies impairs mammalian RNA interference. Nat. Cell Biol. *7*, 1267–1274.

Jonas, S., and Izaurralde, E. (2015). Towards a molecular understanding of microRNA-mediated gene silencing. Nat. Rev. Genet. *16*, 421–433.

Kawamata, T., Seitz, H., and Tomari, Y. (2009). Structural determinants of miRNAs for RISC loading and slicer-independent unwinding. Nat. Struct. Mol. Biol. *16*, 953–960.

Kobayashi, H., and Tomari, Y. (2016). RISC assembly: coordination between small RNAs and Argonaute proteins. Biochim. Biophys. Acta *1859*, 71–81.

Koellner, G., Kryger, G., Millard, C.B., Silman, I., Sussman, J.L., and Steiner, T. (2000). Active-site gorge and buried water molecules in crystal structures of acetylcholinesterase from Torpedo californica. J. Mol. Biol. *296*, 713–735.

Lazzaretti, D., Tournier, I., and Izaurralde, E. (2009). The C-terminal domains of human TNRC6A, TNRC6B, and TNRC6C silence bound transcripts independently of Argonaute proteins. RNA *15*, 1059–1066.

Lee, Y., Ahn, C., Han, J., Choi, H., Kim, J., Yim, J., Lee, J., Provost, P., Rådmark, O., Kim, S., and Kim, V.N. (2003). The nuclear RNase III Drosha initiates microRNA processing. Nature *425*, 415–419.

Levy, Y., and Onuchic, J.N. (2006). Water mediation in protein folding and molecular recognition. Annu. Rev. Biophys. Biomol. Struct. *35*, 389–415.

Liu, P., Harder, E., and Berne, B.J. (2004). On the calculation of diffusion coefficients in confined fluids and interfaces with an application to the liquid-vapor interface of water. J. Phys. Chem. B *108*, 6595–6602.

Liu, J., Carmell, M.A., Rivas, F.V., Marsden, C.G., Thomson, J.M., Song, J.J., Hammond, S.M., Joshua-Tor, L., and Hannon, G.J. (2004a). Argonaute2 is the catalytic engine of mammalian RNAi. Science *305*, 1437–1441.

Liu, J., Rivas, F.V., Wohlschlegel, J., Yates, J.R., 3rd, Parker, R., and Hannon, G.J. (2005a). A role for the P-body component GW182 in microRNA function. Nat. Cell Biol. *7*, 1261–1266.

Liu, J., Valencia-Sanchez, M.A., Hannon, G.J., and Parker, R. (2005b). MicroRNA-dependent localization of targeted mRNAs to mammalian P-bodies. Nat. Cell Biol. *7*, 719–723.

MacRae, I.J., Ma, E., Zhou, M., Robinson, C.V., and Doudna, J.A. (2008). In vitro reconstitution of the human RISC-loading complex. Proc. Natl. Acad. Sci. U S A *105*, 512–517.

Matsumoto, N., Nishimasu, H., Sakakibara, K., Nishida, K.M., Hirano, T., Ishitani, R., Siomi, H., Siomi, M.C., and Nureki, O. (2016). Crystal structure of silkworm PIWI-clade Argonaute Siwi bound to piRNA. Cell *167*, 484–497.e9.

McCoy, A.J., Grosse-Kunstleve, R.W., Adams, P.D., Winn, M.D., Storoni, L.C., and Read, R.J. (2007). Phaser crystallographic software. J. Appl. Cryst. *40*, 658–674.

Meister, G., Landthaler, M., Patkaniowska, A., Dorsett, Y., Teng, G., and Tuschl, T. (2004). Human Argonaute2 mediates RNA cleavage targeted by miRNAs and siRNAs. Mol. Cell *15*, 185–197.

Meyer, E. (1992). Internal water molecules and H-bonding in biological macromolecules: a review of structural features with functional implications. Protein Sci. *1*, 1543–1562.

Michaud-Agrawal, N., Denning, E.J., Woolf, T.B., and Beckstein, O. (2011). MDAnalysis: a toolkit for the analysis of molecular dynamics simulations. J. Comput. Chem. *32*, 2319–2327.

Modzelewski, A.J., Holmes, R.J., Hilz, S., Grimson, A., and Cohen, P.E. (2012). AGO4 regulates entry into meiosis and influences silencing of sex chromosomes in the male mouse germline. Dev. Cell *23*, 251–264.

Nakanishi, K. (2016). Anatomy of RISC: how do small RNAs and chaperones activate Argonaute proteins? Wiley Interdiscip. Rev. RNA *7*, 637–660.

Nakanishi, K., Weinberg, D.E., Bartel, D.P., and Patel, D.J. (2012). Structure of yeast Argonaute with guide RNA. Nature *486*, 368–374.

Nakanishi, K., Ascano, M., Gogakos, T., Ishibe-Murakami, S., Serganov, A.A., Briskin, D., Morozov, P., Tuschl, T., and Patel, D.J. (2013). Eukaryote-specific insertion elements control human ARGONAUTE slicer activity. Cell Rep. *3*, 1893–1900.

Park, S., and Saven, J.G. (2005). Statistical and molecular dynamics studies of buried waters in globular proteins. Proteins *60*, 450–463.

Park, J.H., Shin, S.Y., and Shin, C. (2017a). Non-canonical targets destabilize microRNAs in human Argonautes. Nucleic Acids Res. *45*, 1569–1583.

Park, M.S., Phan, H.D., Busch, F., Hinckley, S.H., Brackbill, J.A., Wysocki, V.H., and Nakanishi, K. (2017b). Human Argonaute3 has slicer activity. Nucleic Acids Res. *45*, 11867–11877.

Pfaff, J., Hennig, J., Herzog, F., Aebersold, R., Sattler, M., Niessing, D., and Meister, G. (2013). Structural features of Argonaute-GW182 protein interactions. Proc. Natl. Acad. Sci. U S A *110*, E3770–E3779.

Phan, H.D., Li, J., Poi, M., and Nakanishi, K. (2018). Quantification of miRNAs co-immunoprecipitated with Argonaute proteins using SYBR green-based qRT-PCR. Methods Mol. Biol. *1680*, 29–40.

Phillips, J.C., Braun, R., Wang, W., Gumbart, J., Tajkhorshid, E., Villa, E., Chipot, C., Skeel, R.D., Kalé, L., and Schulten, K. (2005). Scalable molecular dynamics with NAMD. J. Comput. Chem. *26*, 1781–1802.

Rüdel, S., Wang, Y., Lenobel, R., Körner, R., Hsiao, H.H., Urlaub, H., Patel, D., and Meister, G. (2011). Phosphorylation of human Argonaute proteins affects small RNA binding. Nucleic Acids Res. *39*, 2330–2343.

Sasaki, T., Shiohama, A., Minoshima, S., and Shimizu, N. (2003). Identification of eight members of the Argonaute family in the human genome. Genomics *82*, 323–330.

Schirle, N.T., and MacRae, I.J. (2012). The crystal structure of human Argonaute2. Science *336*, 1037–1040.

Schirle, N.T., Sheu-Gruttadauria, J., and MacRae, I.J. (2014). Structural basis for microRNA targeting. Science *346*, 608–613.

Schirle, N.T., Sheu-Gruttadauria, J., Chandradoss, S.D., Joo, C., and MacRae, I.J. (2015). Water-mediated recognition of t1-adenosine anchors Argonaute2 to microRNA targets. eLife *4*, e07646.

Sheu-Gruttadauria, J., and MacRae, I.J. (2018). Phase transitions in the assembly and function of human miRISC. Cell *173*, 946–957.e16.

Tsuboyama, K., Tadakuma, H., and Tomari, Y. (2018). Conformational activation of Argonaute by distinct yet coordinated actions of the Hsp70 and Hsp90 chaperone systems. Mol. Cell *70*, 722–729.e4.

Wang, Y., Sheng, G., Juranek, S., Tuschl, T., and Patel, D.J. (2008). Structure of the guide-strand-containing argonaute silencing complex. Nature *456*, 209–213.

Williams, M.A., Goodfellow, J.M., and Thornton, J.M. (1994). Buried waters and internal cavities in monomeric proteins. Protein Sci. *3*, 1224–1235.

Winter, J., and Diederichs, S. (2013). Argonaute-3 activates the let-7a passenger strand microRNA. RNA Biol. *10*, 1631–1643.

Yuan, S., Filipek, S., Palczewski, K., and Vogel, H. (2014). Activation of G-protein-coupled receptors correlates with the formation of a continuous internal water pathway. Nat. Commun. *5*, 4733.

Zhang, H., Kolb, F.A., Brondani, V., Billy, E., and Filipowicz, W. (2002). Human Dicer preferentially cleaves dsRNAs at their termini without a requirement for ATP. EMBO J. *21*, 5875–5885.

STAR★METHODS

KEY RESOURCES TABLE

REAGENT or RESOURCE	SOURCE	IDENTIFIER
Antibodies		
Mouse monoclonal anti-FLAG	Sigma-Aldrich	Cat # F1804, RRID: AB_262044
Anti-TNRC6A	Bethyl Laboratories Inc.	Cat # A302-329A, RRID: AB_1850240
Mouse monoclonal anti-α tubulin	Cell Signaling Technology	Cat # 3873T, RRID: AB_1904178
Goat anti-mouse	LI-COR	Cat # 925-32210, RRID: AB_2687825
Goat anti-rabbit	LI-COR	Cat # 925-32211, RRID: AB_2651127
Anti-FLAG M2 beads	Sigma-Aldrich	Cat # A2220, RRID: AB_10063035
Bacterial and Virus Strains		
DH5α competent cells	Invitrogen	Cat # 18258012
One Shot MACH I^{TM} TI	Invitrogen	Cat # 1493679
BL21(DE3) Rosetta2	Novagen	Cat # 71397-3
DH10bac Mar Efficiency	Invitrogen	Cat # 1492020
Chemicals, Peptides, and Recombinant Proteins		
Prime STAR Max premix(2x)	Takara	Cat # R045
Rapid DNA ligation kit	Roche	Cat # 11635379001
Gibson assembly master mix	NEB	Cat # E2611S
Takara Z-taq^{TM}	Takara	Cat # R006A
CellFectin® II reagent	Invitrogen	Cat # 10362-100
TransIt-X2®system	Mirus	Cat # MIR 6006
DpnI	NEB	Cat # R01768
EcoRI	NEB	Cat # R0101T
EcoRV	NEB	Cat # R0195T
NotI	NEB	Cat # 0189S
SigmaFAST^{TM} Protease inhibitor cocktail tablets, EDTA-free	Sigma-Aldrich	Cat # S8830-20TAB
T4PNK	Thermo Scientific	Cat # EK0031
4–12% gradient Bis-Tris gels	Life Technologies	Cat # NW04125BOX
γ-^{32}P-ATP	Parkin-Elmer	Cat # BLU002A250UC
α-^{32}P-GTP	Parkin-Elmer	Cat # BLU006H250UC
Phosphatase, alkaline (AP)	Roche	Cat # 11097975001
Thermo Scientific RiboLock RNase Inhibitor	Thermo Scientific	Cat # E00381
3X FLAG peptides	Sigma-Aldrich	Cat # F4799
Grace's Insect Medium (1x)	GIBCO, Life Technologies	Cat # 11605-094
Penicillin Streptomycin	GIBCO, Life Technologies	Cat # 15070-063
DMEM (Dulbecco's Modified Eagle Medium)	GIBCO, Life Technologies	Cat # 11965-092
FBS (Fetal Bovine Serum, Qualified)	GIBCO, Life Technologies	Cat # 10437-028
Opti-MEM® I	GIBCO, Life Technologies	Cat # 31985-070
0.25% Trypsin-EDTA (1x)	GIBCO, Life Technologies	Cat # 25200-056
ESF 921	Expression Systems	Cat # 96-001-01
Deposited Data		
Human AGO4 Structural data	This paper	PDB: 6OON
Human AGO1 (4KXT)	Nakanishi et al., 2013	PDB: 4KXT
Human AGO1 (4KRE)	Faehnle et al., 2013	PDB: 4KRE
Human AGO1 (4KRF)	Faehnle et al., 2013	PDB: 4KRF

(*Continued on next page*)

Continued

REAGENT or RESOURCE	SOURCE	IDENTIFIER
Human AGO2 (4F3T)	Elkayam et al., 2012	PDB: 4F3T
Human AGO2 (4OLA)	Schirle and MacRae, 2012	PDB: 4OLA
Human AGO2 (4OLB)	Schirle and MacRae, 2012	PDB: 4OLB
Human AGO2 (4Z4D)	Schirle et al., 2015	PDB: 4Z4D
Human AGO2 (6CBD)	Sheu-Gruttadauria and MacRae, 2018	PDB: 6CBD
AGO2 MID domain (3LUC)	Frank et al., 2010	PDB: 3LUC
*Nc*QDE2 (2YHA)	Boland et al., 2011	PDB: 2YHA
Silkworm PIWI-clade Argonaute Siwi (5GUH)	Matsumoto et al., 2016	PDB: 5GUH
Experimental Models: Cell Lines		
Sf9	Expression System	94-001F
Tni	Expression System	94-002F
HEK293T	ATCC	CRL-1573
Oligonucleotides		
AGO4WT-FW-GCGCGCCCATG GAGGCGCTGGGACC	This paper	N/A
AGO4WT-RV-GCGCGCGTCGA CTCAGGCAAA ATAC	This paper	N/A
AGO2Y529E-FW- CGGCAAGACG CCCGTGGAAGCCGAG	This paper	N/A
AGO2Y529E-RV- ACGCGCTTGAC CTCGGCTTCCACGGGC	This paper	N/A
AGO2E637A-FW-GCAGCAGCACC GGCAGGCGATCATACAAG	This paper	N/A
AGO2E637A-RV -GGCGGCCAGG TCTTGTATGATCGCCTGCCGG	This paper	N/A
miR-20a-5p UAAAGUGCUUAU AGUGCAGGUAG	Dharmacon	N/A
miR-20a-3p ACCUGCACUAUA AGCACUUUAAG	Dharmacon	N/A
60-nt miR-20a target RNA GGGA GAAACAAAAAUACCUACCUGC ACUAUAAGCACUUUACCAUCU CAAACUUACUCAGA	Park et al., 2017b	N/A
60-nt miR-20a mismatch target RNA GGGAGAAACAAAAAUACCU ACCUGCACUAAUAGCACUUUA CCAUCUCAAACUUACUCAGA	Dayeh et al., 2018	N/A
Recombinant DNA		
pFB-HTB	Invitrogen	Cat # 10584-027
pCAGEN	Addgene	Cat # 11160
SUMO fused pRSFDuet-1	Dayeh et al., 2018	N/A
Software and Algorithms		
NAMD	http://www.ks.uiuc.edu/Research/namd/	N/A
VMD	http://www.ks.uiuc.edu/Research/vmd/	N/A
MDAnalysis	https://www.mdanalysis.org	N/A
iMOSFLM	https://www.mrc-lmb.cam.ac.uk/harry/imosflm/	N/A
PHASER	McCoy et al., 2007	N/A
PHENIX	www.phenix-online.org/	N/A

(*Continued on next page*)

Continued

REAGENT or RESOURCE	SOURCE	IDENTIFIER
PyMol	https://pymol.org/	N/A
Coot	https://www2.mrc-lmb.cam.ac.uk/personal/pemsley/coot/	N/A
Chimera	https://www.cgl.ucsf.edu/chimera/	N/A
imageQuant	https://www.gelifesciences.com/en/us/shop/protein.../imagequant-tl-8-1-p-00110	N/A
Image studio	https://www.licor.com/bio/image-studio/	N/A
Prism	https://www.graphpad.com/scientific-software/prism/	N/A
imageJ	https://imagej.nih.gov	N/A

LEAD CONTACT AND MATERIALS AVAILABILITY

Further information and requests for resources and reagents should be directed to and will be fulfilled by the lead contact Kotaro Nakanishi (nakanishi.9@osu.edu).

EXPERIMENTAL MODEL AND SUBJECT DETAILS

HEK293T cells were cultured in Dulbecco's modified Eagle's medium (DMEM, GIBCO) supplemented with 10% (v/v) Fetal Bovine Serum (FBS, Sigma-Aldrich) and 1% (v/v) Penicillin-Streptomycin (GIBCO) at 37°C with 5% CO_2. Plasmids were transfected by TransIT-X2 reagent (Mirus). For the AGO4 overexpression, Sf9 and *Trichoplusia ni* (Tni) cells were used for Bac-to-Bac Baculovirus Expression System. Sf9 and Tni cells were grown in Grace's Insect Medium (GIBCO) and ESF 921(Expression Systems). Refer the KEY Resources Table for detail information of cell strains and medium.

METHOD DETAILS

Cloning, expression, and purification of AGO proteins and TNRC6B fragments

Recombinant AGO2 and AGO4 were purified from insect cells as previously reported (Park et al., 2017b). TNRC6B fragments were cloned into a SUMO-fused pRSFDuet-1 vector (Novagen) and plasmids were transformed into BL21(DE3) *E. coli* cells. SUMO-fused TNRC6B fragments were purified by two steps. After the homogenized cells were centrifuged for 1 hour, the supernatant was loaded onto 5 mL HisTrap HP column (GE Healthcare) equilibrated with Buffer A (10 mM phosphate buffer pH 7.3, 1 M NaCl, 40 mM imidazole, 10 mM β-mercaptoethanol, 5% glycerol). The column was washed with Buffer A, followed by elution of the fragments over a linear gradient to 50% of Buffer B (10 mM phosphate buffer pH 7.3, 1 M NaCl, 1.5 M imidazole, 10 mM β-mercaptoethanol, 5% glycerol). The eluted samples were dialyzed against Buffer C (200 mM NaCl, 20 mM Tris-HCl pH 7.5, 10 mM β-mercaptoethanol) and then concentrated by ultrafiltration. The concentrated proteins were loaded onto HiLoad 16/600 Superdex 75 column (GE Healthcare) equilibrated with Buffer D (20 mM Tris-HCl pH 7.5, 200 mM NaCl, 2 mM Dithiothreitol (DTT)). After concentration by ultrafiltration, the purified SUMO-fused TNRC6B fragments were flash-frozen in liquid nitrogen and stored at −80°C. For *in vitro* cleavage assays, a gene of FLAG-tagged AGO2 was cloned into a pCAGEN vector (Addgene). Mutants were subsequently generated from this construct by site-directed mutagenesis with primers that were designed to anneal to the mutation site. The PCR products were digested by Dpn1 (NEB) and then transformed into DH5α *E. coli* cells (Invitrogen™). The mutations were verified by sequencing. In our western blot analyses, all chimeras and mutants of AGO showed comparable expression levels in HEK293T cells without degradation, indicating that they were properly folded.

Crystallization, structure determination and refinement

The purified AGO4 in Buffer E (10 mM Tris-HCl pH 8.0, 200 mM NaCl, 5 mM DTT) was crystallized at 20°C using the sitting-drop vapor diffusion method in 450 mM lithium chloride, 100 mM MES buffer pH 6.0, 16% PEG6,000, 15 mM trimethylamine. Crystals were soaked in cryoprotectant buffer (450 mM lithium chloride, 100 mM MES buffer pH 6.0, 16% PEG6,000, 15 mM trimethylamine, 20% (v/v) glycerol) and cryo-cooled in liquid nitrogen. Data were collected at the NE-CAT beamlines (Advanced Photon Source, Chicago) and processed with iMOSFLM (Battye et al., 2011). Molecular replacement was performed with PHASER (McCoy et al., 2007) using the crystal structure of AGO2 (PDB ID: 4OLA) as the search model. The structural model was refined using PHENIX (Adams et al., 2010). All figures of structures and electrostatic surfaces were generated using PyMol (http://www.pymol.org/) and Chimera (https://www.cgl.ucsf.edu/chimera/).

Cell culture, transfection, cell lysis and western blot

HEK293T cells were cultured in Dulbecco's modified Eagle's medium (DMEM, GIBCO) supplemented with 10% (v/v) Fetal Bovine Serum (FBS, Sigma-Aldrich) and 1% (v/v) Penicillin-Streptomycin (GIBCO) under standard condition (37°C and 5% CO_2). 10 μg of pCAGEN plasmid encoding the FLAG-tagged AGO protein was transfected into one 10 cm plate using the TransIT-X2 reagent (Mirus). Cells were harvested and weighed 48 hours after transfection. Cell pellets were resuspended in five-fold excess volume (v/w) of Lysis Buffer (30 mM HEPES-KOH pH 7.4, 100 mM KOAc, 2 mM $Mg(OAc)_2$, 1 mM DTT, 1 mM phenylmethylsulfonyl fluoride, EDTA-free protease inhibitor cocktail), and lysed by ultrasonication. Cell lysate (7 μl) was used for western blot analysis. 5 μl of SDS loading buffer (125 mM Tris–HCl pH 6.8, 4% sodium dodecyl sulfate (SDS), 20% Glycerol, 0.04% Bromophenol blue, and 100 mM β-mercaptoethanol) was mixed with the same volume of the cell lysates and incubated at 90°C for 1 min. The sample was separated on 4%–12% gradient Bis-Tris gels (Life Technologies) and transferred to Amersham Hybond ECL nitrocellulose membranes (GE Healthcare). Anti-FLAG antibody (F1804, Sigma-Aldrich, 1:1000 dilution), anti-TNRC6A antibody (A302-329A, BETHLY, 1:1000 dilution), anti-mouse antibody (IRDye 800CW Goat anti-Mouse IgG, LI-COR, 1:16 000 dilution), and anti-rabbit antibody (IRDye 800CW Goat anti-Rabbit IgG, LI-COR, 1:16 000 dilution) were used as the primary and the secondary antibodies. The amount of FLAG-AGO proteins in the cell lysate was normalized by western blot result, AGO was quantified by using a standard curve generated with known amounts of recombinant FLAG-AGO3.

In vitro cleavage assay

An siRNA-like duplex of miR-20a and a 60-nt 5′ cap-labeled target RNA were prepared as previously reported (Park et al., 2017b). Based on the western blot data, 50 pmol of AGO mutants were incubated with 0.5 pmol of an siRNA duplex of miR-20a at 37°C for 1 hour for the RISC assembly, followed by immunoprecipitation (IP) with 20 μl of anti-FLAG M2 beads (Sigma-Aldrich) for 2 hours at room temperature. The beads were washed eight times with IP-Wash Buffer (30 mM HEPES-KOH pH 7.4, 300 mM NaCl, 100 mM KOAc, 2 mM $Mg(OAc)_2$, 1% Triton X-100) and two times with 1x Cleavage Buffer (25 mM HEPES-KOH pH 7.4, 50 mM KOAc, 5 mM $Mg(OAc)_2$, 5 mM DTT). The cleavage reaction was initiated by adding 0.5 pmol of 5′ cap-labeled target RNAs in 1x cleavage buffer and 5 U/μL RiboLock RNase Inhibitor (ThermoFisher) at 37°C for 1 hour. The reaction was stopped by adding 20 μl of quenching dye (7 M urea, 1 mM EDTA, 0.05% (w/v) xylene cyanol, 0.05% (w/v) bromophenol blue, 10% (v/v) phenol). Cleavage products were resolved on a 7 M urea denaturing 16% (w/v) polyacrylamide gel. The gels were dried on filter paper and analyzed by phosphorimaging.

RISC maturation assay

pCAGEN vector encoding either of FLAG-AGO mutants were transfected into HEK293T cells as previously reported (Park et al., 2017b). After 48 hours, 50 mg of the harvested cells were resuspended in 300 μL of Lysis Buffer (1% NP-40, 150 mM NaCl, 25 mM Tris-HCl pH 7.5, 2 mM EDTA, 0.5 mM DTT, 0.1% SDS, and 0.1% sodium deoxycholate). The cells were lysed with ultrasonication and centrifuged at 15,000 × *g* for 20 min at 4°C. 5 μL of the lysate was resolved on an SDS-PAGE, and the FLAG-AGO mutant was detected by western blot with anti FLAG antibody (Sigma-Aldrich). The amount of the FLAG-AGO mutant was quantified using a standard curve of recombinant FLAG-AGO3. The lysate was adjusted so as to contain 50 pmol of FLAG-AGO mutant and then incubated with 5 pmol of siRNA-like duplex of miR-20a whose guide strand was radiolabeled at its 5′ end for 1 hour at 37°C. Then, FLAG-AGO mutant was immunoprecipitated with 60 μL of anti-FLAG M2 beads (Sigma-Aldrich) for 2 hours at room temperature. The beads were washed 8 times with Wash Buffer (300 mM NaCl, 50 mM Tris-HCl pH 7.5, 5 mM $MgCl_2$, and 0.05% NP-40) and 2 times with Cleavage Buffer (25 mM HEPES-KOH pH 7.5, 50 mM KCl, 5 mM $MgCl_2$, 5 mM DTT, and 2 mM EDTA). AGO-bound RNAs were extracted from the beads using 200 μL of phenol-chloroform and then precipitated with ethanol. After centrifugation, the RNA pellets were dissolved with 10 μL of 1 × Annealing Buffer (30 mM HEPES-KOH pH 7.5, 100 mM KOAc, 1 mM EDTA) and native loading dye (15% w/v of Ficoll, 2 mM $MgCl_2$, 0.5 TBE). The samples were resolved on a 10% native gel to separate the single-stranded guide RNA from the duplex. The intensity of pre-RISC (i.e., a complex of AGO with a duplex) and of mature RISC (i.e., a complex of AGO with a guide) are $I_{pre\text{-}RISC}$ and I_{RISC}, respectively. The relative duplex loading and passenger ejection were calculated with these equations;

$$I_{total} = I_{pre-RISC} + I_{RISC}$$

$$I_{total}(WT) = I_{pre-RISC}(WT) + I_{RISC}(WT)$$

$$I_{total}(mut) = I_{pre-RISC}(mut) + I_{RISC}(mut)$$

$$Relative\ duplex\ loading = \frac{I_{total}(mut)}{I_{total}(WT)}$$

$$passenger\ ejection = \frac{I_{pre-RISC}}{I_{total}}$$

Filter binding assay

FLAG-AGO mutant (50 pmol) was incubated with 5 pmol of siRNA-like duplex of miR-20a for 1 hour at 37°C and immunoprecipitated with anti-FLAG M2 beads for 2 hours at room temperature. After the beads were thoroughly washed with Wash Buffer as described in the RISC maturation assay, FLAG-AGO mutant was eluted with 250 μg/ml of FLAG peptide (Sigma-Aldrich) overnight at 4°C. The eluted AGO mutant was incubated with a 60-nt 5′ cap-labeled mismatch target (GGGAGAAACAAAAAUACCUACCUGCACUAAUAG CACUUUACCAUCUCAAACUUACUCAGA) for 1 hour at 37°C. After the reactions were put on Hybond ECL nitrocellulose membranes (GE Healthcare) and Zeta-Probe Blotting Membranes (BIO-RAD), the membranes were washed with 1 × Binding Buffer (25 mM HEPES-KOH pH 7.5, 10 mM $MgCl_2$, 3 mM DTT, and 125 mM $NaCl_2$) and analyzed by phosphorimager.

Binding assay with TNRC6 fragments

The binding assays were performed with a Superdex 200 increase 10/300 GL column (GE Healthcare) equilibrated with Buffer F (150 mM NaCl, 20 mM Tris-HCl pH 7.5, 2 mM DTT). The column was injected with 2 nmol of AGO protein, of a SUMO-fused TNRC6 fragment, or their mixture incubated on ice for 30 min.

Simulation systems preparation

The crystallographic structures of human AGO4 (PDB ID: 6OON) and AGO2 (PDB ID: 4OLA) were used to build the systems for simulations (Table S2). Missing loops were not added and their ends were treated as non-neutral N and C termini. Hydrogen atoms were automatically added to protein structures and crystallographic water molecules. Residues aspartate, glutamate, lysine, and arginine were assumed to be charged. Histidine residues were assumed neutral, and their protonation state was chosen to favor the formation of evident hydrogen bonds. Additional water molecules and randomly placed ions were used to solvate the systems with 150 mM NaCl. Two systems were built for AGO4: i) $AGO4_{CW}$ protein + RNA + crystallographic water molecules, and ii) $AGO4_{NCW}$ protein + RNA and no crystallographic waters inside of the LAKE1 cavity. For AGO2 only one system was built: $AGO2_{CW}$ protein + RNA + crystallographic waters. All systems were built using the psfgen, solvate and ionize plugins of VMD (Humphrey et al., 1996).

MD simulations

All MD simulations were performed using NAMD 2.11 (Phillips et al., 2005), the CHARMM36 force field for proteins and nucleic acids with the CMAP correction and the TIP3P model for water (Huang and MacKerell, 2013). A cutoff of 12 Å (with a switching function starting at 10 Å) was used for van der Waals interactions along with periodic boundary conditions. The Particle Mesh Ewald method was used to compute long-range electrostatic forces without cutoff and with a grid point density of > 1 $Å^{-3}$. A uniform 2 fs integration time step was used together with SHAKE. Langevin dynamics was utilized to enforce constant temperature ($T = 300$ or $T = 310$ K) with a damping coefficient of 0.1 ps^{-1} unless otherwise stated. Constant pressure simulations (*NpT*) at 1 atm were conducted using the hybrid Nosé-Hoover Langevin piston method with a 200 fs decay period and a 50 fs damping time constant. Initially the $AGO4_{NCW}$, $AGO4_{CW}$ and $AGO2_{CW}$ systems were subjected to 5000 steps of minimization followed by 200 ps of dynamics with the backbone of the protein and the C2′ atoms of the RNA restrained and by 1 ns of free dynamics in the *NpT* ensemble ($T = 300$ K, p = 1 atm, Langevin damping coefficient $\gamma = 1$ ps^{-1}).

Definition of LAKE1 and LAKE2 for estimation of water dynamics parameters from the MD trajectories

Carefully tailored selections were defined for AGO4 and AGO2 in order to precisely monitor the water molecules that reside inside LAKE1 and LAKE2 during the MD simulations and to avoid the inclusion of water molecules that are outside of the cavities. Water molecules were considered to be inside the cavity if their oxygen atom was located within 4 Å of a selection of atoms. For LAKE1 of AGO4 this selection includes the side-chain atoms of residues 567, 568 and 858, the side-chain OH group of residue 617 or the backbone oxygen atoms of residues 565, 614, 615 and 795. Similarly for LAKE1 of AGO2 the selection includes the side-chain atoms of residue 576 and 623, the side-chain OH group of residues 625 and 805 or the backbone oxygen of residues 573, 622, 787, 789, 790, 791, 793, and 795. LAKE2 of AGO4 includes the side-chain atoms of residues 719, 725, 732, 761, and 764, the Cβ atom of residue 362 or the backbone atoms of residue 716. For AGO2, LAKE2 includes side-chain atoms of residue 730, the Cβ atom of residue 372 or the backbone atoms of residues 714, 715, 717 and 728.

Computation of survival probability of water molecules in MD simulations

Local translational and rotational mobility of water molecules can be related to the amount of time that a molecule is likely to remain in a given region (Liu et al., 2004a). By measuring which fraction of molecules were in a given region at time *t* and remain there at a later time $t+\tau$, the survival probability $P(\tau)$ can be computed. The decay rate of $P(\tau)$ depends on the size of the region and the mobility of molecules within it and is calculated as follows:

$$P(\tau) = \frac{1}{T_n} \sum_{t}^{T_n} \frac{N(t,\tau)}{N(t)}$$

where $N(t,\tau)$ is the number of particles that remain in the selection at time $t + \tau$, $N(t)$ is the number of particles at time t, and T_n is the number of time steps contributing to $P(\tau)$.

The survival probability was calculated from our trajectories using the water dynamics module of the MD-analysis library (Araya-Secchi et al., 2014; Gowers et al., 2016; Michaud-Agrawal et al., 2011). Each $P(\tau)$ was estimated for all the available time windows (τ = 1 to 100 ps) from four 20 ns segments of the 100 ns simulations excluding the first 20 ns. The data presented in Figure 3C corresponds to $P(\tau)$ averaged for each time window.

QUANTIFICATION AND STATISTICAL ANALYSIS

All the assay data were quantified using ImageJ (https://imagej.nih.gov/ij/) and ImageQuant (GE Healthcare life Sciences). The dot plots in Figures 1, 3, and 5 were generated by Prism software (GraphPad) and black bars on the graph show averages with independent replicates shown as dots. The detail calculations were in the method section.

DATA AND CODE AVAILABILITY

The accession number for the crystal structure of human AGO4 reported in this paper is PDB: 6OON.

Molecular Cell, Volume *75*

Supplemental Information

Multidomain Convergence of Argonaute during RISC Assembly Correlates with the Formation of Internal Water Clusters

Mi Seul Park, Raul Araya-Secchi, James A. Brackbill, Hong-Duc Phan, Audrey C. Kehling, Ekram W. Abd El-Wahab, Daniel M. Dayeh, Marcos Sotomayor, and Kotaro Nakanishi

Molecular Cell, Volume *XX*

Supplemental Information

Multidomain Convergence of Argonaute During RISC Assembly Correlates with the Formation of Internal Water Clusters

Mi Seul Park, Raul Araya-Secchi, James A. Brackbill, Hong-Duc Phan, Audrey C. Kehling, Ekram W. Abd El-Wahab, Daniel M. Dayeh, Marcos Sotomayor, and Kotaro Nakanishi

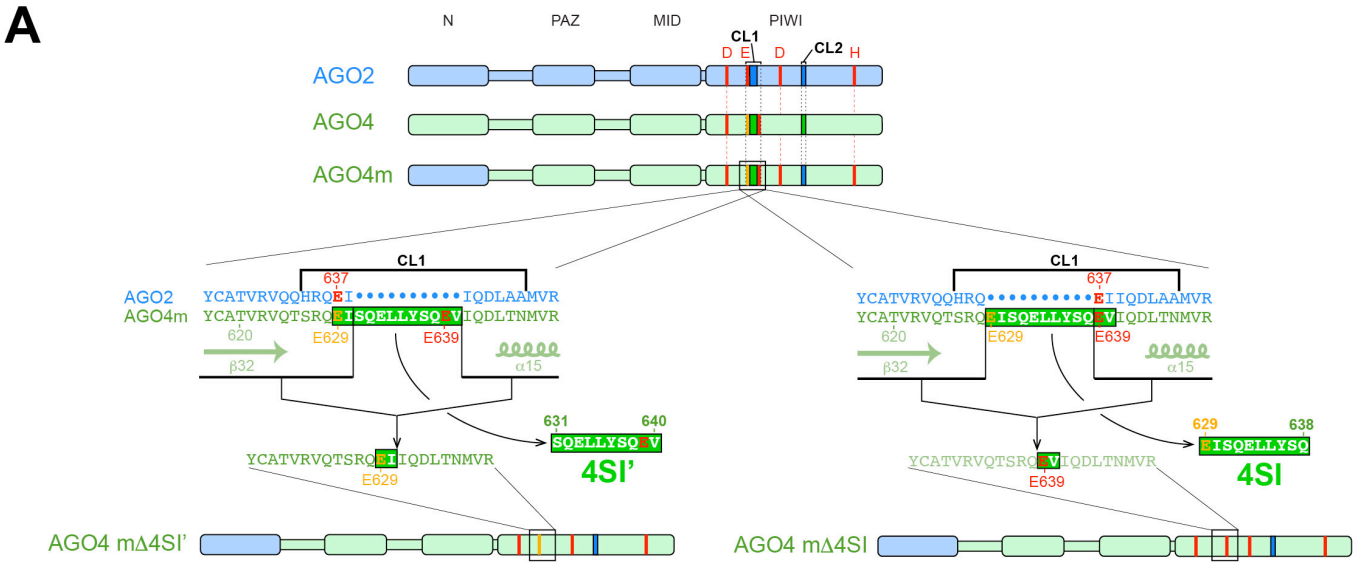
A
N
PAZ
MID
PIWI
CL1
CL2
D E
D
H
AGO2
AGO4
AGO4m
CL1
637
AGO2 YCATVRVQQHRQEI••••••••••IQDLAAMVR
AGO4m YCATVRVQTSRQEISQELLYSQEVIQDLTNMVR
620
β32
E629
E639
α15
631
640
SQELLYSQEV
YCATVRVQTSRQEIIQDLTNMVR
E629
4SI'
AGO4 mΔ4SI'
CL1
637
YCATVRVQQHRQ••••••••••EIIQDLAAMVR
YCATVRVQTSRQEISQELLYSQEVIQDLTNMVR
620
β32
E629
E639
α15
629
638
EISQELLYSQ
YCATVRVQTSRQEVIQDLTNMVR
E639
4SI
AGO4 mΔ4SI

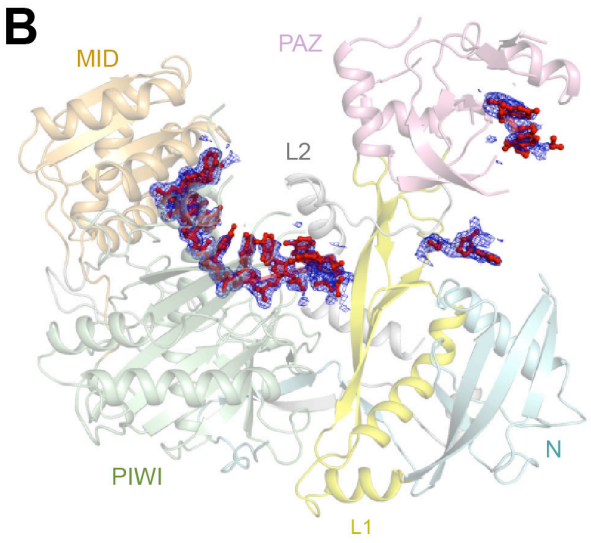
B
MID
PAZ
L2
N
PIWI
L1

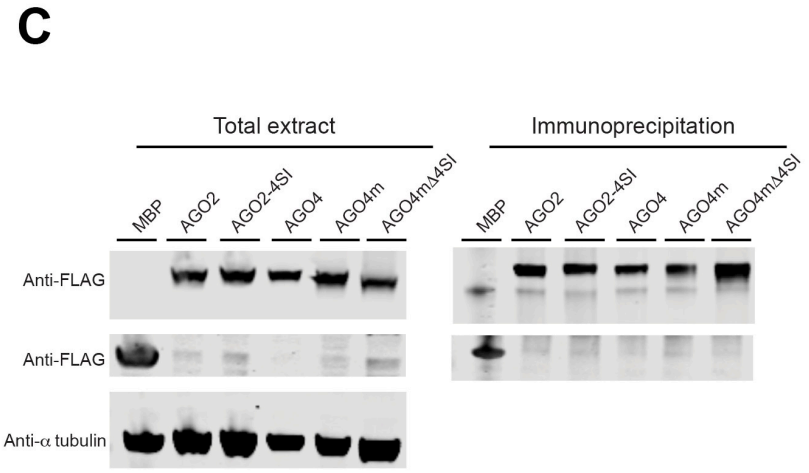
C
Total extract
Immunoprecipitation
MBP
AGO2
AGO2-4SI
AGO4
AGO4m
AGO4mΔ4SI
Anti-FLAG
Anti-FLAG
Anti-α tubulin

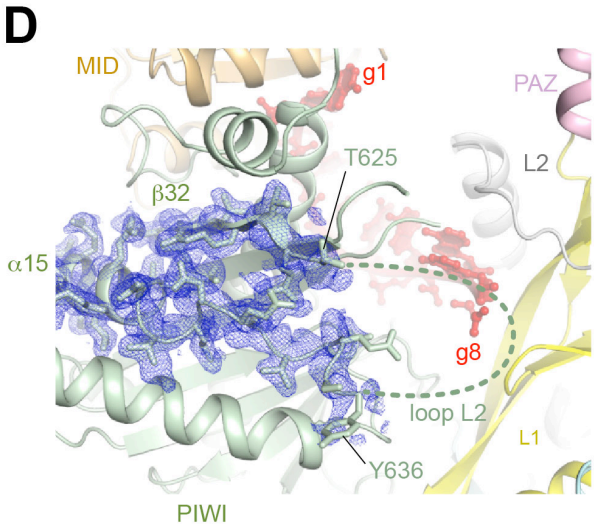
D
MID
g1
PAZ
T625
L2
β32
α15
g8
loop L2
L1
Y636
PIWI

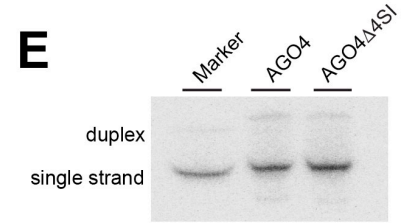
E
Marker
AGO4
AGO4Δ4SI
duplex
single strand

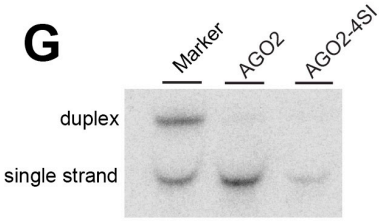
G
Marker
AGO2
AGO2-4SI
duplex
single strand

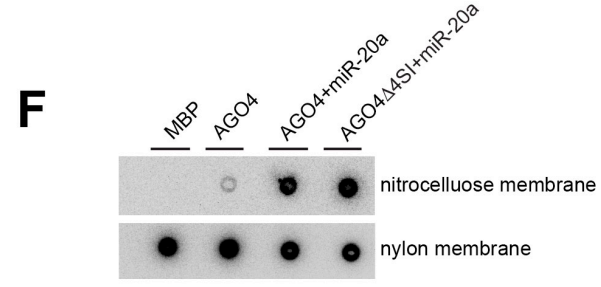
F
MBP
AGO4
AGO4+miR-20a
AGO4Δ4SI+miR-20a
nitrocelluose membrane
nylon membrane

Figure S1. Strategy for making AGO4 into a catalytically active enzyme (Related to Figure 1)

(A) Differences in the construct used by Hauptmann *et al.* (left) and that used in the current study (right), both of which generate a catalytically active AGO4 mutant.

(B) Simulated annealing F_o-F_c omit map contoured at 2.5 σ (blue mesh) around the guide RNA. Colors as in Figure 1B.

(C) FLAG-AGO2, FLAG-AGO4 and their mutants were expressed in HEK293T cells and detected with anti-FLAG antibody (left). Their protein amounts were adjusted based on the western blot (right) and used for target cleavage assay (Figure 1E).

(D) Simulated annealing F_o-F_c omit map contoured at 2.2 σ (blue mesh) around α15 and β32 of AGO4. The disordered loop L2, including 4SI, is depicted as dotted lines. Colors as in (B).

(E) RISC maturation assays of AGO4 and AGO4Δ4SI (Figure 1H and 1I). The lysates of HEK293T cells expressing either FLAG-AGO4 or FLAG-AGO4Δ4SI were adjusted by western blot so as to include 50 pmol of AGO, followed by incubation with miR-20a duplex. The duplex is composed of a 5′ end labeled miR-20a and a fully complementary passenger strand that lacks a 5' monophosphate. After immunoprecipitation with anti-FLAG beads, the AGO-bound RNAs were extracted and resolved on 10% native gel.

(F) Filter binding assay of MBP, AGO4, and AGO4Δ4SI. The lysates of HEK293T cells expressing either FLAG-MBP, FLAG-AGO4 or FLAG-AGO4Δ4SI were incubated with miR-20a duplexes and then immunoprecipitated with anti-FLAG beads. After the AGOs were eluted from the beads with FLAG peptides, the AGOs were incubated with 60-nt 5′ cap labeled mismatch targets. The resultants were spotted on a nitrocellulose membrane and a nylon membrane. AGO4 without miR-20a was used as a control to subtract the non-specific bound targets (Figure 1J).

(G) RISC maturation assays of AGO2 and AGO2-4SI (Figure 1K). The lysates of HEK293T cells expressing either FLAG-AGO2 or FLAG-AGO2-4SI were adjusted by western blot so as to include 50 pmol of AGO, followed by incubation with miR-20a duplex. The duplex is composed of a 5′ end labeled miR-20a and a fully complementary passenger strand that lacks a 5’ monophosphate. After immunoprecipitation with anti-FLAG beads, the AGO-bound RNAs were extracted and resolved on 10% native gel.

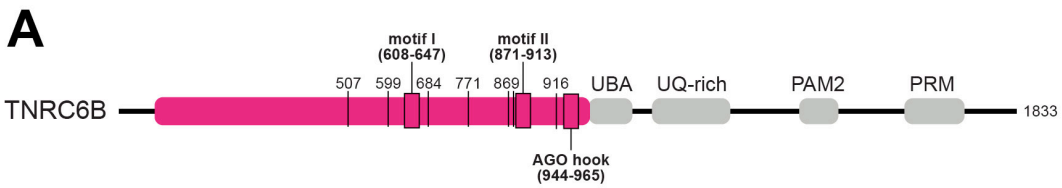
A
motif I
(608-647)
motif II
(871-913)
507
599
684
771
869
916
UBA
UQ-rich
PAM2
PRM
TNRC6B
1833
AGO hook
(944-965)

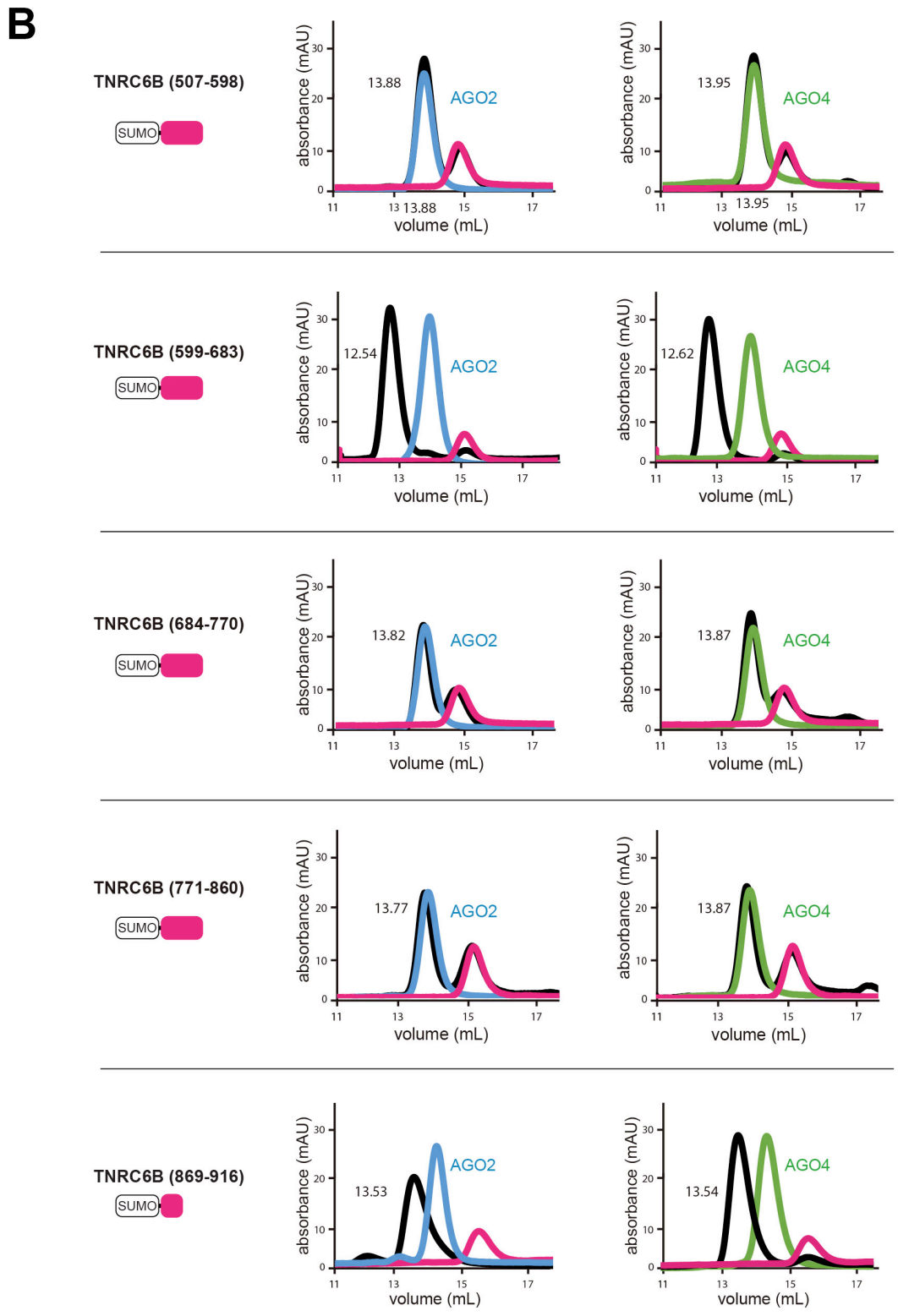
B
TNRC6B (507-598)
SUMO
absorbance (mAU)
13.88
AGO2
volume (mL)
13.95
AGO4
TNRC6B (599-683)
12.54
12.62
TNRC6B (684-770)
13.82
13.87
TNRC6B (771-860)
13.77
13.87
TNRC6B (869-916)
13.53
13.54

Figure S2. Interactions of long TNRC6B fragments with AGO2 and AGO4 (Related to Figure 2)

(A) Domain architecture of TNRC6B. Several long fragments were designed from the AGO-binding regions (pink) and expressed as SUMO-fused proteins.

(B) Gel filtration analyses of AGO2 (blue), AGO4 (green), SUMO-fused TNRC6B fragment (pink), and a mixture of a TNRC6B fragment with either AGO2 or AGO4 (black).

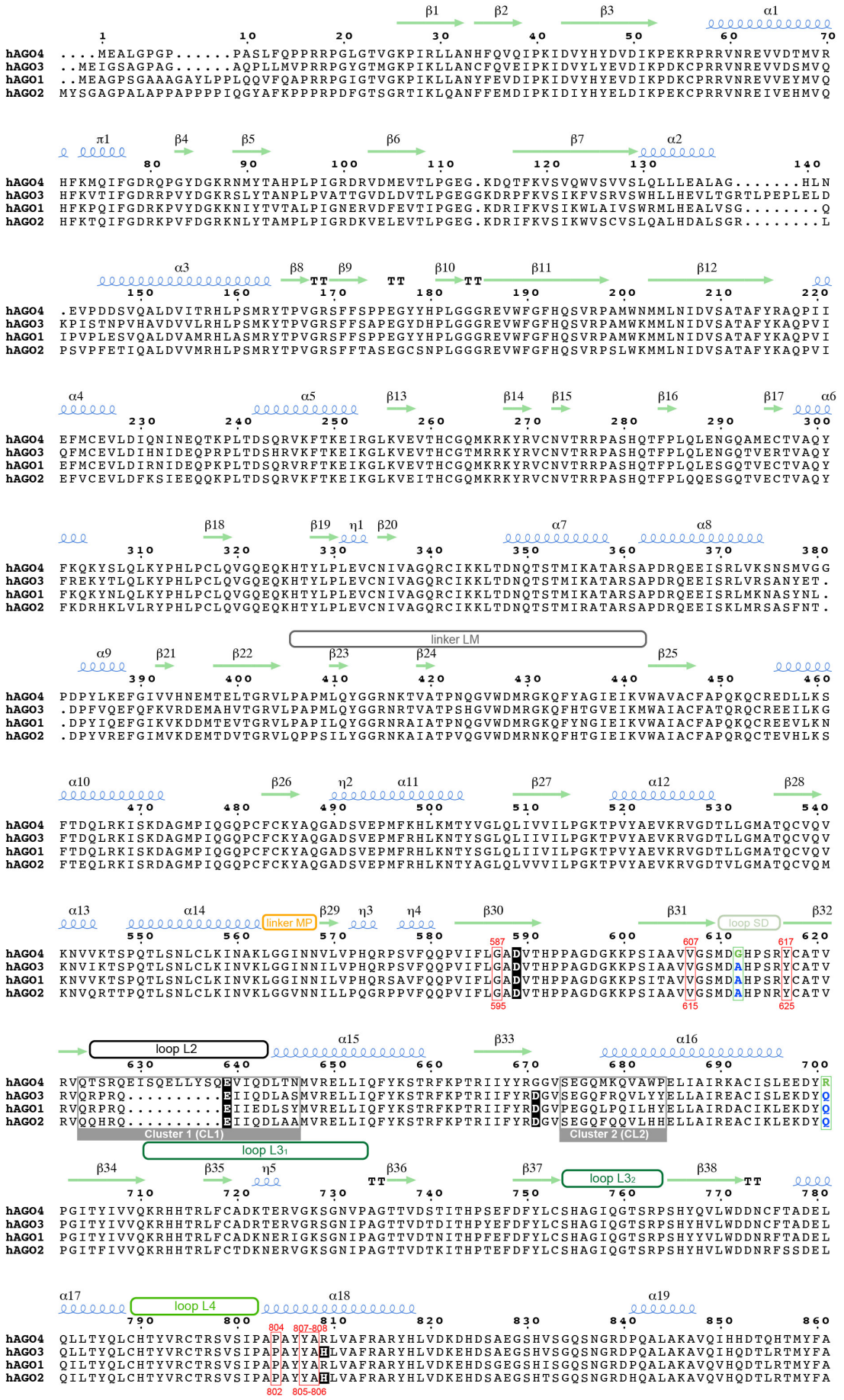
β1 β2 β3 α1
1 10 20 30 40 50 60 70
hAGO4 ....MEALGPGP......PASLFQPPRRPGLGTVGKPIRLLANHFQVQIPKIDVYHYDVDIKPEKRPRRVNREVVDTMVR
hAGO3 ..MEIGSAGPAG......AQPLLMVPRRPGYGTMGKPIKLLANCFQVEIPKIDVYLYEVDIKPDKCPRRVNREVVDSMVQ
hAGO1 ..MEAGPSGAAAGAYLPPLQQVFQAPRRPGIGTVGKPIKLLANYFEVDIPKIDVYHYEVDIKPDKCPRRVNREVVEYMVQ
hAGO2 MYSGAGPALAPPAPPPPIQGYAFKPPPRPDFGTSGRTIKLQANFFEMDIPKIDIYHYELDIKPEKCPRRVNREIVEHMVQ
π1 β4 β5 β6 β7 α2
80 90 100 110 120 130 140
hAGO4 HFKMQIFGDRQPGYDGKRNMYTAHPLPIGRDRVDMEVTLPGEG.KDQTFKVSVQWVSVVSLQLLLEALAG.......HLN
hAGO3 HFKVTIFGDRRPVYDGKRSLYTANPLPVATTGVDLDVTLPGEGGKDRPFKVSIKFVSRVSWHLLHEVLTGRTLPEPLELD
hAGO1 HFKPQIFGDRKPVYDGKKNIYTVTALPIGNERVDFEVTIPGEG.KDRIFKVSIKWLAIVSWRMLHEALVSG........Q
hAGO2 HFKTQIFGDRKPVFDGRKNLYTAMPLPIGRDKVELEVTLPGEG.KDRIFKVSIKWVSCVSLQALHDALSGR........L
α3 β8 β9 β10 β11 β12
TT TT TT
150 160 170 180 190 200 210 220
hAGO4 .EVPDDSVQALDVITRHLPSMRYTPVGRSFFSPPEGYYHPLGGGREVWFGFHQSVRPAMWNMMLNIDVSATAFYRAQPII
hAGO3 KPISTNPVHAVDVVLRHLPSMKYTPVGRSFFSAPEGYDHPLGGGREVWFGFHQSVRPAMWKMMLNIDVSATAFYKAQPVI
hAGO1 IPVPLESVQALDVAMRHLASMRYTPVGRSFFSPPEGYYHPLGGGREVWFGFHQSVRPAMWKMMLNIDVSATAFYKAQPVI
hAGO2 PSVPFETIQALDVVMRHLPSMRYTPVGRSFFTASEGCSNPLGGGREVWFGFHQSVRPSLWKMMLNIDVSATAFYKAQPVI
α4 α5 β13 β14 β15 β16 β17 α6
230 240 250 260 270 280 290 300
hAGO4 EFMCEVLDIQNINEQTKPLTDSQRVKFTKEIRGLKVEVTHCGQMKRKYRVCNVTRRPASHQTFPLQLENGQAMECTVAQY
hAGO3 QFMCEVLDIHNIDEQPRPLTDSHRVKFTKEIKGLKVEVTHCGTMRRKYRVCNVTRRPASHQTFPLQLENGQTVERTVAQY
hAGO1 EFMCEVLDIRNIDEQPKPLTDSQRVRFTKEIKGLKVEVTHCGQMKRKYRVCNVTRRPASHQTFPLQLESGQTVECTVAQY
hAGO2 EFVCEVLDFKSIEEQQKPLTDSQRVKFTKEIKGLKVEITHCGQMKRKYRVCNVTRRPASHQTFPLQQESGQTVECTVAQY
β18 β19 η1 β20 α7 α8
310 320 330 340 350 360 370 380
hAGO4 FKQKYSLQLKYPHLPCLQVGQEQKHTYLPLEVCNIVAGQRCIKKLTDNQTSTMIKATARSAPDRQEEISRLVKSNSMVGG
hAGO3 FREKYTLQLKYPHLPCLQVGQEQKHTYLPLEVCNIVAGQRCIKKLTDNQTSTMIKATARSAPDRQEEISRLVRSANYET.
hAGO1 FKQKYNLQLKYPHLPCLQVGQEQKHTYLPLEVCNIVAGQRCIKKLTDNQTSTMIKATARSAPDRQEEISRLMKNASYNL.
hAGO2 FKDRHKLVLRYPHLPCLQVGQEQKHTYLPLEVCNIVAGQRCIKKLTDNQTSTMIRATARSAPDRQEEISKLMRSASFNT.
linker LM
α9 β21 β22 β23 β24 β25
390 400 410 420 430 440 450 460
hAGO4 PDPYLKEFGIVVHNEMTELTGRVLPAPMLQYGGRNKTVATPNQGVWDMRGKQFYAGIEIKVWAVACFAPQKQCREDLLKS
hAGO3 .DPFVQEFQFKVRDEMAHVTGRVLPAPMLQYGGRNRTVATPSHGVWDMRGKQFHTGVEIKMWAIACFATQRQCREEILKG
hAGO1 .DPYIQEFGIKVKDDMTEVTGRVLPAPILQYGGRNRAIATPNQGVWDMRGKQFYNGIEIKVWAIACFAPQKQCREEVLKN
hAGO2 .DPYVREFGIMVKDEMTDVTGRVLQPPSILYGGRNKAIATPVQGVWDMRNKQFHTGIEIKVWAIACFAPQRQCTEVHLKS
α10 β26 η2 α11 β27 α12 β28
470 480 490 500 510 520 530 540
hAGO4 FTDQLRKISKDAGMPIQGQPCFCKYAQGADSVEPMFKHLKMTYVGLQLIVVILPGKTPVYAEVKRVGDTLLGMATQCVQV
hAGO3 FTDQLRKISKDAGMPIQGQPCFCKYAQGADSVEPMFRHLKNTYSGLQLIIVILPGKTPVYAEVKRVGDTLLGMATQCVQV
hAGO1 FTDQLRKISKDAGMPIQGQPCFCKYAQGADSVEPMFRHLKNTYSGLQLIIVILPGKTPVYAEVKRVGDTLLGMATQCVQV
hAGO2 FTEQLRKISRDAGMPIQGQPCFCKYAQGADSVEPMFRHLKNTYAGLQLVVVILPGKTPVYAEVKRVGDTVLGMATQCVQM
α13 α14 linker MP β29 η3 η4 β30 β31 loop SD β32
550 560 570 580 590 600 610 620
587 607 617
hAGO4 KNVVKTSPQTLSNLCLKINAKLGGINNVLVPHQRPSVFQQPVIFLGADVTHPPAGDGKKPSIAAVVGSMDGHPSRYCATV
hAGO3 KNVIKTSPQTLSNLCLKINVKLGGINNILVPHQRPSVFQQPVIFLGADVTHPPAGDGKKPSIAAVVGSMDAHPSRYCATV
hAGO1 KNVVKTSPQTLSNLCLKINVKLGGINNILVPHQRSAVFQQPVIFLGADVTHPPAGDGKKPSITAVVGSMDAHPSRYCATV
hAGO2 KNVQRTTPQTLSNLCLKINVKLGGVNNILLPQGRPPVFQQPVIFLGADVTHPPAGDGKKPSIAAVVGSMDAHPNRYCATV
595 615 625
loop L2 α15 β33 α16
630 640 650 660 670 680 690 700
hAGO4 RVQTSRQEISQELLYSQEVIQDLTNMVRELLIQFYKSTRFKPTRIIYYRGGVSEGQMKQVAWPELIAIRKACISLEEDYR
hAGO3 RVQRPRQ.........EIIQDLASMVRELLIQFYKSTRFKPTRIIFYRDGVSEGQFRQVLYYELLAIREACISLEKDYQ
hAGO1 RVQRPRQ.........EIIEDLSYMVRELLIQFYKSTRFKPTRIIFYRDGVPEGQLPQILHYELLAIRDACIKLEKDYQ
hAGO2 RVQQHRQ.........EIIQDLAAMVRELLIQFYKSTRFKPTRIIFYRDGVSEGQFQQVLHHELLAIREACIKLEKDYQ
Cluster 1 (CL1) Cluster 2 (CL2)
loop L3₁
β34 β35 η5 β36 β37 loop L3₂ β38
TT TT
710 720 730 740 750 760 770 780
hAGO4 PGITYIVVQKRHHTRLFCADKTERVGKSGNVPAGTTVDSTITHPSEFDFYLCSHAGIQGTSRPSHYQVLWDDNCFTADEL
hAGO3 PGITYIVVQKRHHTRLFCADRTERVGRSGNIPAGTTVDTDITHPYEFDFYLCSHAGIQGTSRPSHYHVLWDDNCFTADEL
hAGO1 PGITYIVVQKRHHTRLFCADKNERIGKSGNIPAGTTVDTNITHPFEFDFYLCSHAGIQGTSRPSHYYVLWDDNRFTADEL
hAGO2 PGITFIVVQKRHHTRLFCTDKNERVGKSGNIPAGTTVDTKITHPTEFDFYLCSHAGIQGTSRPSHYHVLWDDNRFSSDEL
α17 loop L4 α18 α19
790 800 810 820 830 840 850 860
804 807-808
hAGO4 QLLTYQLCHTYVRCTRSVSIPAPAYYARLVAFRARYHLVDKDHDSAEGSHVSGQSNGRDPQALAKAVQIHHDTQHTMYFA
hAGO3 QLLTYQLCHTYVRCTRSVSIPAPAYYAHLVAFRARYHLVDKEHDSAEGSHVSGQSNGRDPQALAKAVQIHQDTLRTMYFA
hAGO1 QILTYQLCHTYVRCTRSVSIPAPAYYARLVAFRARYHLVDKEHDSGEGSHISGQSNGRDPQALAKAVQVHQDTLRTMYFA
hAGO2 QILTYQLCHTYVRCTRSVSIPAPAYYAHLVAFRARYHLVDKEHDSAEGSHTSGQSNGRDHQALAKAVQVHQDTLRTMYFA
802 805-806

Figure S3. Sequence alignment of human AGO paralogs (Related to Figure 2; Figure 3; Figure 4)
Residue number and secondary structure of AGO4 are shown above the sequence. The four catalytic residues are highlighted with black columns. AGO4-specific residues in Trp Pocket-2 and -3 are boxed (green). Residues involved in van der Waals interactions between two PIWI subdomains are boxed (red). Domain linkers and loops forming LAKE1 and LAKE2 are labeled above the sequence. CL1 and CL2 are boxed (gray).

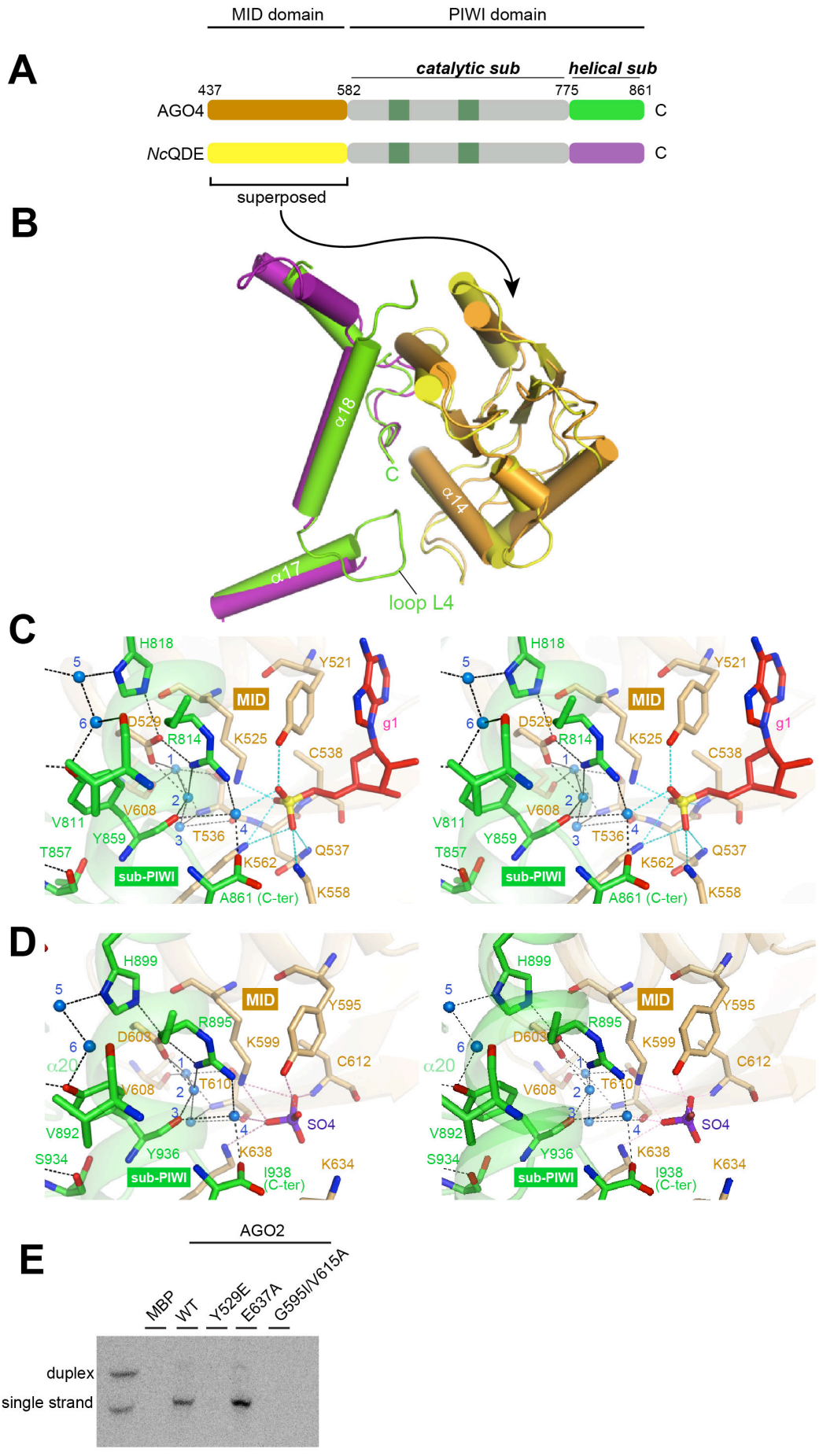
MID domain
PIWI domain
A
catalytic sub
helical sub
437
582
775
861
AGO4
C
NcQDE
C
superposed
B
α18
C
α14
α17
loop L4
C
H818
Y521
MID
D529
R814
K525
g1
C538
V608
V811
Y859
T536
T857
sub-PIWI
K562
Q537
A861 (C-ter)
K558
D
H899
Y595
R895
D603
K599
C612
α20
T610
SO4
V892
S934
Y936
K638
K634
I938
(C-ter)
E
AGO2
MBP
WT
Y529E
E637A
G595I/V615A
duplex
single strand

Figure S4. Interactions between MID domain and PIWI-helical subdomain (Related to Figure 3; Figure 4)

(A) MID-PIWI domain architectures of AGO4 and *Nc*QDE2.

(B) Superposition of AGO4 and *Nc*QDE2 on their MID domains results in a good alignment of their PIWI-helical subdomains.

(C-D) Stereoviews of the interactions between the MID domain and PIWI-helical subdomain in AGO4 (C) and *Nc*QDE2 (D). Colors as in (A). Water molecules and hydrogen bonds are depicted as spheres (cyan) and dotted lines, respectively. For clarity, only g1 of the bound guide RNA is shown in (C). The bound sulfate ion is drawn as a stick model (magenta) in (D).

(E) A representative image of RISC maturation assay with siRNA duplex (Figure 3E).

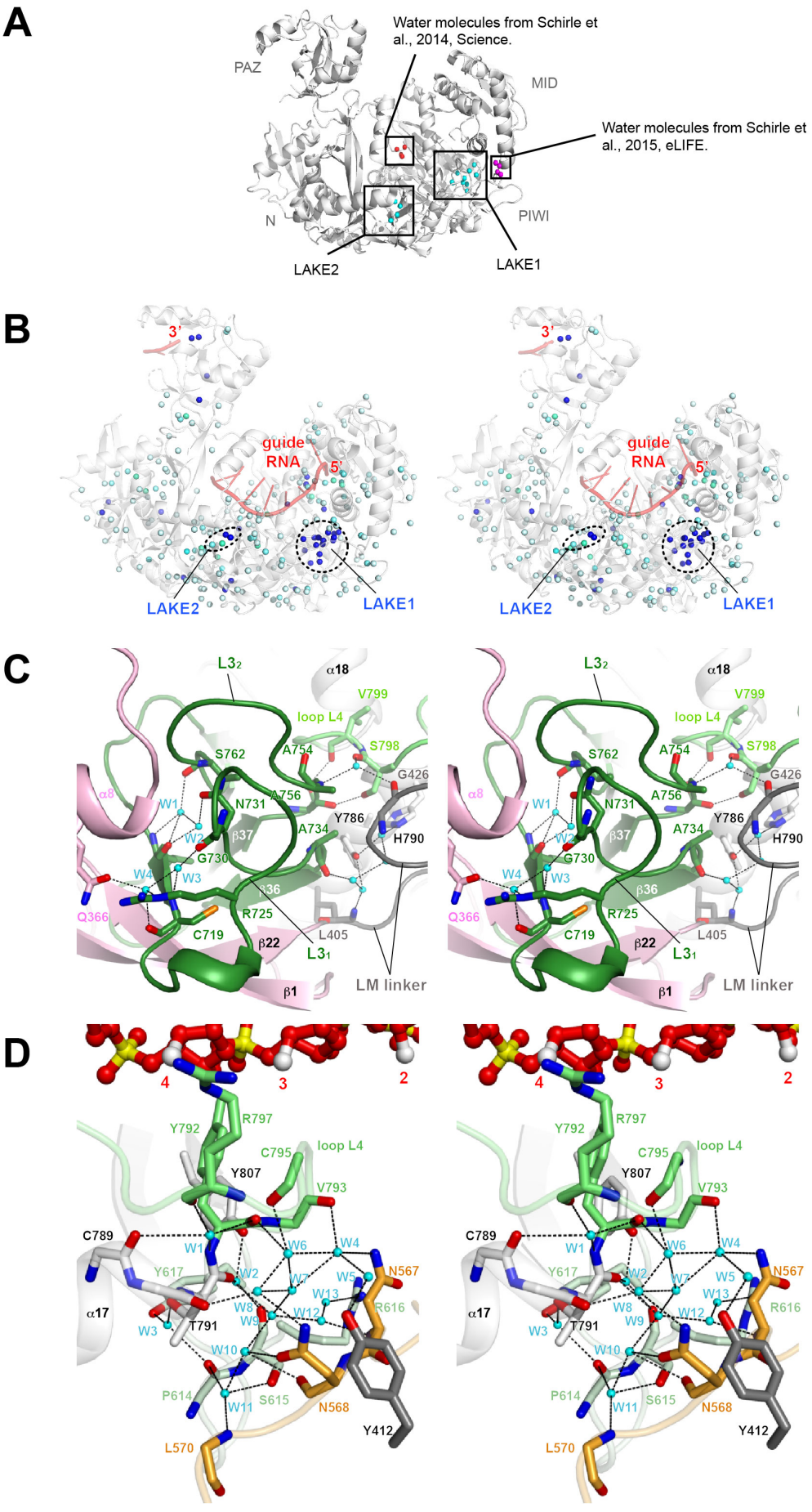
A
Water molecules from Schirle et al., 2014, Science.
PAZ
MID
Water molecules from Schirle et al., 2015, eLIFE.
N
PIWI
LAKE2
LAKE1
B
3'
guide RNA
5'
LAKE2
LAKE1
3'
guide RNA
5'
LAKE2
LAKE1
C
L3₂
α18
V799
loop L4
S762
A754
S798
G426
α8
W1
N731
A756
Y786
W2
β37
A734
H790
G730
W4
W3
β36
Q366
R725
C719
β22
L405
L3₁
β1
LM linker
L3₂
α18
V799
loop L4
S762
A754
S798
G426
α8
W1
N731
A756
Y786
W2
β37
A734
H790
G730
W4
W3
β36
Q366
R725
C719
β22
L405
L3₁
β1
LM linker
D
4
3
2
Y792
R797
C795
loop L4
Y807
V793
C789
W1
W6
W4
Y617
W2
W7
W5
N567
W13
α17
W8
R616
T791
W9
W12
W3
W10
P614
W11
S615
N568
Y412
L570
4
3
2
Y792
R797
C795
loop L4
Y807
V793
C789
W1
W6
W4
Y617
W2
W7
W5
N567
W13
α17
W8
R616
T791
W9
W12
W3
W10
P614
W11
S615
N568
Y412
L570

Figure S5. Water-mediated hydrogen-bonding network (Related to Figure 5)

(A) Locations of LAKEs (cyan) and the previously reported water molecules at the active site (red) and the target nucleotide-1 pocket (magenta).

(B) Stereoview of water molecules bound to AGO4. The intensity of the blue color indicates the categories of the water molecule. Dark blue, cyan, and faint blue spheres indicate buried, cleft, and surface water molecules, respectively.

(C-D) Stereoview of the internal water-mediated hydrogen-bonding network in LAKE2 (C) and LAKE1 (D). Water molecules and hydrogen bonds are depicted as cyan spheres and dotted lines, respectively. The bound RNA in (D) is drawn as a ball-and-stick model. Colors as in Figure 4C.

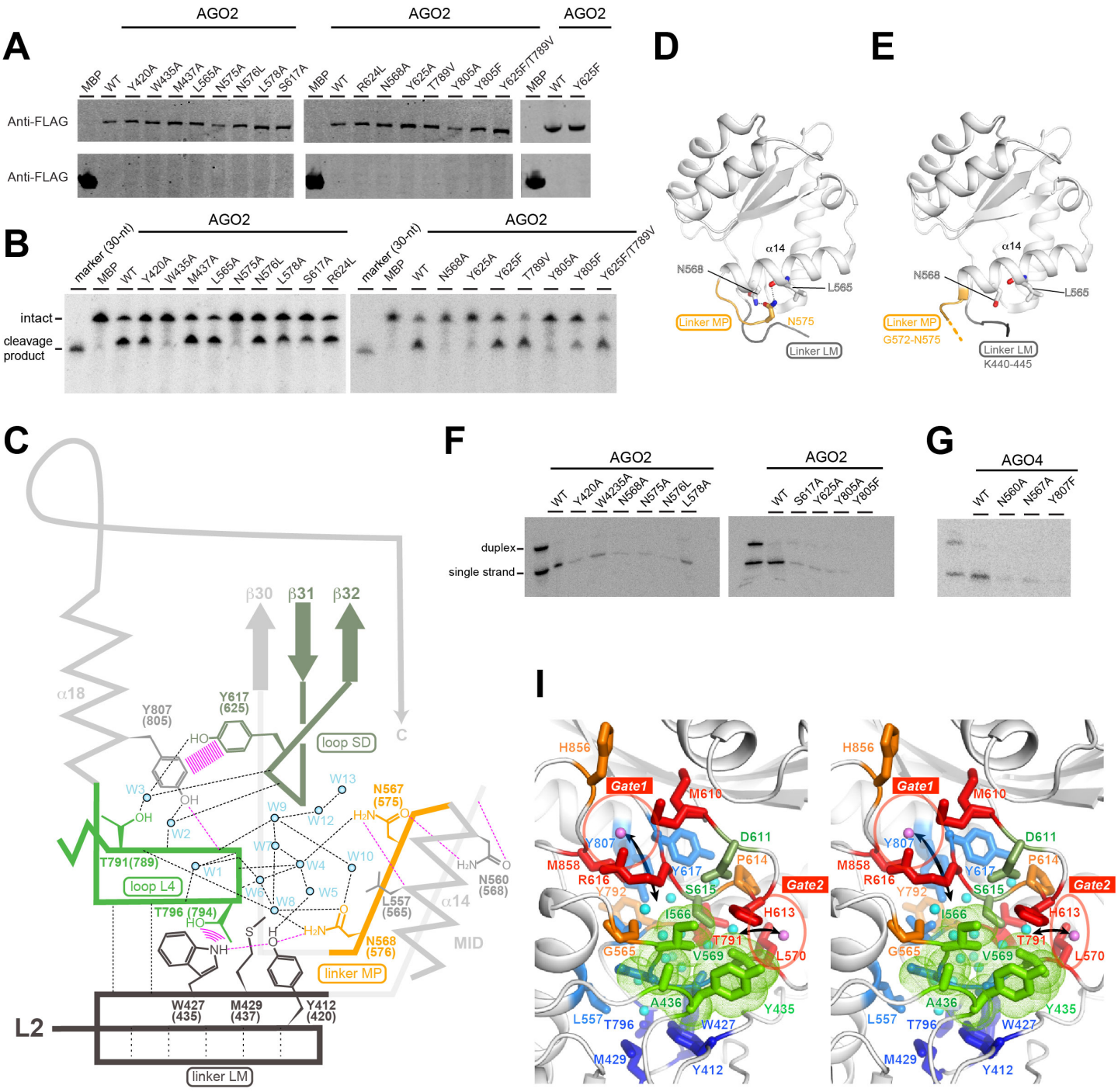

Figure S6. Residues and their interactions required for LAKE1 formation (Related to Figure 5)

(A) A representative image of western blot analysis with anti-FLAG antibody. Expression levels of mutants were tested, and the amount of proteins were adjusted for the target cleavage assay.

(B) A representative image of *In vitro* cleavage assay with miR-20a. All lysates were adjusted by western blots of (A) and the 5 μM AGO proteins were incubated with 50 nM siRNA-like duplex of miR-20a for RISC assembly. 50 nM 5' cap-labeled target RNAs were used for the RNA cleavage reaction.

(C) A schematic of LAKE1. Conserved residues involved in the LAKE1 formation are shown. The internal water molecules and hydrogen bonds are depicted as spheres (cyan) and dotted lines (black), respectively. Hydrogen bonds not involving water molecules are colored in pink.
(D-E) Interactions between the MID domain and linker MP through two asparagine residues seen in the full-length AGO2 (D) (PDB ID: 4OLA) but not in the isolated AGO2 MID domain (E) (PDB ID: 3LUC).
(F-G) A representative image of RISC maturation assays with siRNA-like duplex of miR-20a (Figure 5H-5J).
(I) Stereoview of the two gates, Gate1 and Gate 2 (red circles), of the AGO4 LAKE1. Water molecules inside LAKE1 are colored in cyan. Two water molecules located just outside the two gates are colored in pink. Residues shaping the AGO4 LAKE1 can be categorized based on their roles; back wall (dark blue), middle wall (marine), gates (red), hydrophobic core (green), backbone (orange).

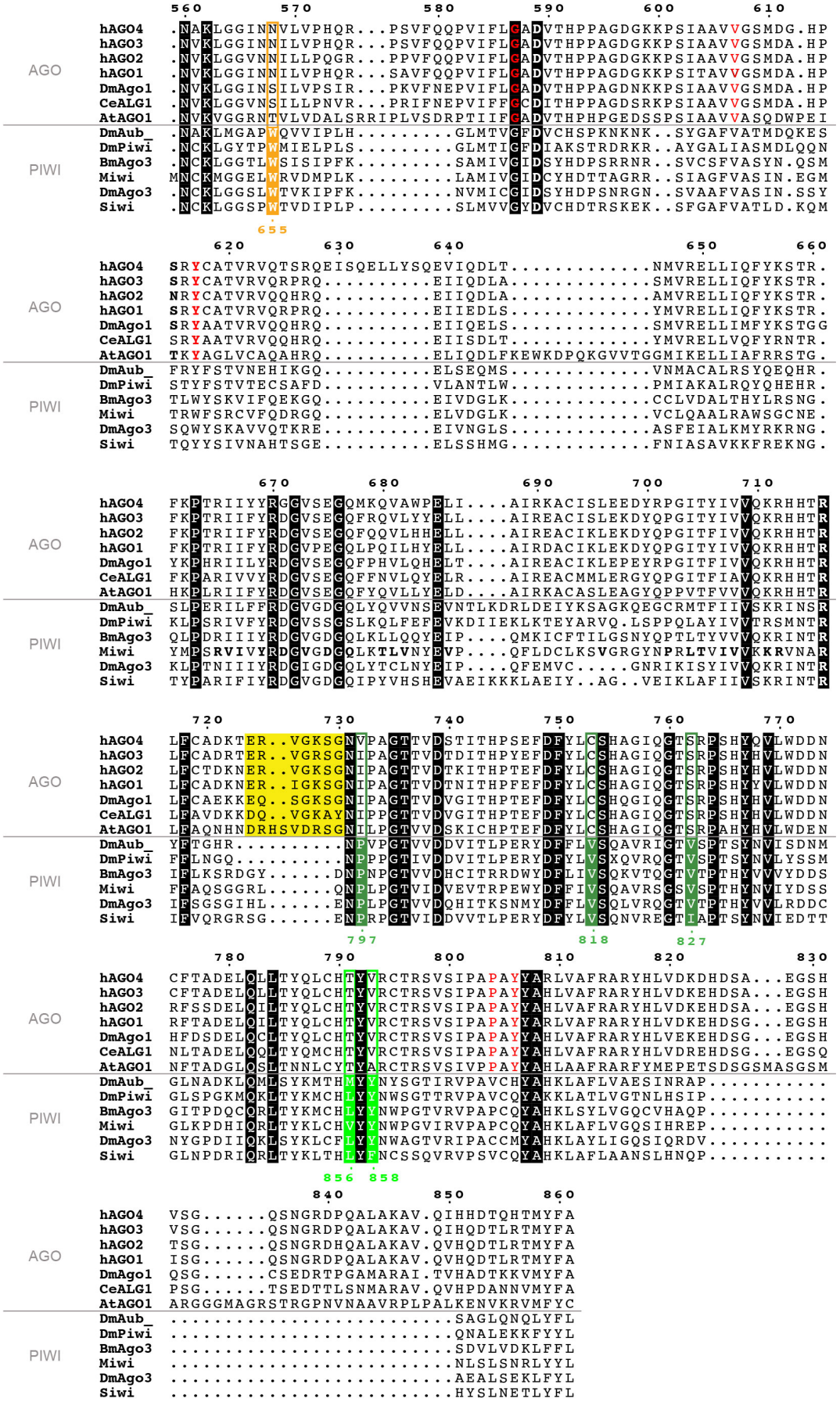
AGO
PIWI
hAGO4
hAGO3
hAGO2
hAGO1
DmAgo1
CeALG1
AtAGO1
DmAub_
DmPiwi
BmAgo3
Miwi
DmAgo3
Siwi

Figure S7. Sequence alignment of AGO- and PIWI-clade proteins (Related to Figure 7)

Residues highlighted in red participate in the van der Waals interaction between two PIWI subdomains. Residues in colored boxes (linker MP: orange, $L3_1$ and $L3_2$: dark green, loop L4: bright green) have different properties between AGO and PIWI clades. Residue numbers of AGO4 and Siwi are shown above and below the sequence alignment, respectively. AGO-specific insert in $L3_1$ is colored in yellow (see Figure 7C-D).

Table S1. Detailed simulation statistics of LAKE1 and LAKE2 of $AGO2_{cw}$ and $AGO4_{cw}$ (Related to Figure 6)

AGO and Temp	Number of water molecules							Avg. Occup.*	t_1 (ps)	t_2 (ps)
	Cavity	Mean	SD	Variance	max	min	median			
AGO4cw 300 K	LAKE1	10.3	1.8	3.2	18	5	10	10 ± 2	34.6	3.6
	LAKE2	7.3	1.6	2.7	18	3	7	7 ± 2	-	-
AGO4cw 310 K	LAKE1	10.2	1.5	2.3	18	6	10	10 ± 2	31.4	3.2
	LAKE2	6.1	1.1	1.3	11	2	6	6 ± 1	-	-
AGO2cw 300 K	LAKE1	12.7	1.4	2.1	19	8	13	13 ± 1	42.2	3.5
	LAKE2	4.7	0.8	0.6	8	2	5	5 ± 1	-	-
AGO2cw 310 K	LAKE1	12.6	2.0	4.0	23	6	13	13 ± 2	25	2.8
	LAKE2	5.7	0.8	0.7	10	3	6	6 ± 1	-	-

*Correspond to rounded up values of the mean ± sd number of water molecules in columns 3 and 4

Table S2. Details of simulated systems (Related to Simulation systems preparation section of STAR Methods)

System	#	PDB	t_{sim} (ns)	Type	Ensemble	Temp (K)	Start	Size #atoms	Size (nm^3)
AGO4cw	S1a	6OON	1.21	MinEQ	*NpT**	300	------	164,443	12x12x12
AGO4cw	S1b	6OON	100	EQ	*NpT*	300	S1a	164,443	12x12x12
AGO4cw	S1c	6OON	100	EQ	*NpT*	310	S1a	164,443	12x12x12
AGO4ncw	S2a	6OON	1.21	MinEQ	*NpT**	300	------	164,443	12x12x12
AGO4ncw	S2b	6OON	100	EQ	*NpT*	300	S2a	164,443	12x12x12
AGO4ncw	S2c	6OON	61	EQ	*NpT*	310	S2a	164,443	12x12x12
AGO2cw	S3a	4OLA	1.21	MinEQ	*NpT**	300	------	164,230	12x12x12
AGO2cw	S3b	4OLA	100	EQ	*NpT*	300	S3a	164,230	12x12x12
AGO2cw	S3c	4OLA	100	EQ	*NpT*	310	S3a	164,230	12x12x12

Summary of all MD simulations**.** Asterisk (*) denotes simulations that consisted of 5000 steps of minimization, 200 ps of dynamics with the backbone of the protein restrained (k_{bbr} = 1 kcal mol^{-1} $Å^{-2}$), and 1 ns of free dynamics in the *NpT* ensemble (γ = 1 ps^{-1}).

Table S3. Primer list (Related to Cloning, expression, and purification of AGO proteins and TNRC6B fragment section of STAR Methods)

Oligonucleotides	Source	Identifier
AGO2G595I/V615A-FW-CAGCAGCCCGTCATCTTTCTGATAGCAGACGTCAC, CCATTGCCGCCGTGGCGGGCAGCATGGACGCC	This paper	N/A
AGO2G595I/V615A-RV - GGCGTCCATGCTGCCCGCCACGGCGGCAATGG, GGCGTCCATGCTGCCCGCCACGGCGGCAATGG	This paper	N/A
AGO2Y420A-FW-GCCGCCCTCCATCCTCGCCGGGGGCAGGAATAAAGC	This paper	N/A
AGO2Y420A-RV - GCTTTATTCCTGCCCCCGGCGAGGATGGAGGGCGGC	This paper	N/A
AGO2W435A-FW-CCCTGTCCAGGGCGTCGCGGACATGCGGAACAAGCAGT	This paper	N/A
AGO2W435A-RV - ACTGCTTGTTCCGCATGTCCGCGACGCCCTGGACAGGG	This paper	N/A
AGO2L565A-FW-CAGACCCTGTCCAACCTCTGCGCGAAGATCAACGTCAAGCTGGGA	This paper	N/A
AGO2L565A-RV - TCCCAGCTTGACGTTGATCTTCGCGCAGAGGTTGGACAGGGTCTG	This paper	N/A
AGO2N568A-FW-GTCCAACCTCTGCCTGAAGATCGCCGTC	This paper	N/A
AGO2N568A-RV - CGCCTCCCAGCTTGACGGCGATCTTCAGGCA	This paper	N/A
AGO2N575A-FW-GTCAAGCTGGGAGGCGTGGCCAAC	This paper	N/A
AGO2N575A-RV - CTGGGGCAGCAGGATGTTGGCCACGCCTCCC	This paper	N/A
AGO2 L578A -FW-CTGGGAGGCGTGAACAACATCGCGCTGCCCCAGGGCAGG	This paper	N/A
AGO2 L578A -RV - CCTGCCCTGGGGCAGCGCGATGTTGTTCACGCCTCCCAG	This paper	N/A
AGO2S617A -FW-CCGCCGTGGTGGGCGCCATGGACGCCCACCCC	This paper	N/A
AGO2S617A -RV - GGGGTGGGCGTCCATGGCGCCCACCACGGCGG	This paper	N/A
AGO2Y625A -FW- CGCCCACCCCAATCGCGCCTGC	This paper	N/A
AGO2Y625A -RV - CGCACGGTGGCGCAGGCGCGATTGGG	This paper	N/A
AGO2Y805A-FW-TCCCAGCCAGCATACGCCGCTC	This paper	N/A
AGO2Y805A-RV - GGCCACCAGGTGAGCGGCGTATGCTGGCG	This paper	N/A
AGO2-4SI-FW-TGCAGCAGCACCGGCAGGAGATCTCCCAAGAGCTCCTCTACAGTCAAGA	This paper	N/A
AGO2-4SI-RV - GCGGCCAGGTCTTGTATGATCTCTTGACTGTAGAGGAGCTCTTGG	This paper	N/A

AGO4m-FW-GACTTCCCGGCAGGAGATCTCCCAAGAGCTCCTCTACAGTCAAGA, GACTTCCCGGCAGGAGATCTCCCAAGAGCTCCTCTACAGTCAAGA, GGAGGGGTATCTGAGGGACAATTCCAGCAGGTTCTCCACCACGAGTTGCTGGCCATCCGTG	This paper	N/A
AGO4m-RV -AACCATGTTAGTCAGGTCCTGGATGACCTCTTGACTGTAGAGGAGCTCTTGG, CTTGCCCTAAATGCTACAAGATGGGCATAATATGCAGGGGC, GGCCGGTAATCTTCTTCCAACTTGATACAGGCCTCACGGATGGCCAGCAACT	This paper	N/A
AGO4mΔ4SI-FW-GTGCAGACTTCCCGGCAGGAGGTCATCCAGGACCTGACTAA	This paper	N/A
AGO4mΔ4SI-RV-TTAGTCAGGTCCTGGATGACCTCCTGCCGGGAAGTCTGCAC	This paper	N/A
TNRC6B-599-683-FW-GCGCGCCTCGAGTCAGAGCTCCCCCCATCCAGA	This paper	N/A
TNRC6B-599-683-RV-GCGCGCGGATCCGATTGTCAGGCTGTCTTGCAGA	This paper	N/A
TNRC6B-507-598-FW-GCGCGCGGATCCTCTCAGGGAGAATGGAAACAGC	This paper	N/A
TNRC6B-507-598-RV-GCGCGCCTCGAGTCAAGGATGTGTGGGCCTGTACG	This paper	N/A
TNRC6B-684-770-FW-GCGCGCGGATCCTCAGCCTCTACAGAGTGGAAAGACC	This paper	N/A
TNRC6B-684-770-RV-GCGCGCCTCGAGTCAAGACACAGGTTTACTTGCAGAACTTTC	This paper	N/A
TNRC6B-771-860-FW-GCGCGCGGATCCGGGTGGGGTGAAGGAGGG	This paper	N/A
TNRC6B-771-860-RV-GCGCGCCTCGAGTCACTCCAGCTGGAATTGGAAGG	This paper	N/A
TNRC6B-869-916-FW-GCGCGCGGATCCACTGTGGATAATGGTACTTCAGCATG	This paper	N/A
TNRC6B-869-916-RV-GCGCGCAAGCTTTCAGGGTTCCCCCCAGCTGG	This paper	N/A
TNRC6B-616-636-FW-CAAATTAAGCAGGACACAGTGTGGTGACTCGAGTCTGGTAAAGAAACCG	This paper	N/A
TNRC6B-616-636-RV-CGGTTTCTTTACCAGACTCGAGTCACCACACTGTGTCCTGCTTAATTTG	This paper	N/A
TNRC6B-623-636-FW-ACAGAGAACAGATTGCTGCATCCTGGGGCCAAACTCAAATTAAGC	This paper	N/A
TNRC6B-623-636-RV-GCTTAATTTGAGTTTGGCCCCAGGATGCAGCAATCTGTTCTCTGT	This paper	N/A
TNRC6B-617-634-FW-GCGCGCGGATCCGTGCTCTCAAACACTGGCTGGG	This paper	N/A
TNRC6B-617-634-RV-GCGCGCCTCGAGTCAAATGTCCCACACTGTGTCCTGC	This paper	N/A

TNRC6B-617-634(Q625E)-FW-TCAAACACTGGCTGGGGCGAAACTCAAATTAAGCAGGACACAGTGT	This paper	N/A
TNRC6B-617-634(Q625E)-RV-ACACTGTGTCCTGCTTAATTTGAGTTTCGCCCCAGCCAGTGTTTGA	This paper	N/A
TNRC6B-617-634(K629A)-FW-GCTGGGGCCAAACTCAAGCTAAGCAGGACACAGTGTGGGA	This paper	N/A
TNRC6B-617-634(K629A)-RV-TCCCACACTGTGTCCTGCTTAGCTTGAGTTTGGCCCCAGC	This paper	N/A
TNRC6B-617-634(Q630R)-FW-GGGGCCAAACTCAAATTAAGCGGGACACAGTGTGGGACATTTGA	This paper	N/A
TNRC6B-617-634(Q630R)-RV-TCAAATGTCCCACACTGTGTCCCGCTTAATTTGAGTTTGGCCCC	This paper	N/A